




Microscopic calculations of nuclear level densities with the Lanczos methodW. E. Ormand ^{1,2,*} and B. A. Brown ²¹*Lawrence Livermore National Laboratory, P.O. Box 808, L-414, Livermore, California 94551, USA*²*Department of Physics and the National Superconducting Cyclotron Laboratory,
Michigan State University, East Lansing, Michigan 42284-1321, USA* (Received 4 March 2018; revised 19 December 2019; accepted 17 June 2020; published 23 July 2020)

A new method for computing the density of states in nuclei making use of an extrapolated form of the tridiagonal matrix obtained from the Lanczos method is presented. It will be shown that the global, average properties of the entire Lanczos matrix can be predicted from just four Lanczos iterations. The extrapolated Lanczos matrix (ELM) approach provides for an accurate computation of the density of states described within the configuration space, which, in some cases, is sufficient to accurately calculate the density of states at, or near, the neutron separation energy. Comparisons between theory and experiment are shown for ^{57}Fe , ^{74}Ge , and ^{76}Ge . In addition, we show results for the J -dependence of moments and the level density for these three nuclei.

DOI: [10.1103/PhysRevC.102.014315](https://doi.org/10.1103/PhysRevC.102.014315)**I. INTRODUCTION**

The density of states is a fundamental property of nuclear structure and plays a key role in nuclear reactions. An important example is the radiative capture of neutrons on short-lived nuclei, which, through the r -process [1] in supernovae and/or neutron-star mergers [2], are thought to be responsible for the synthesis of the elements heavier than iron. Ideally, these reactions can be measured or constrained by experiment. Unfortunately, in most cases, the target nuclei are so short lived that direct measurement is not possible, and the only alternative is to rely on theoretical calculations or indirect measurements such as surrogates [3], which are themselves reliant on theoretical input.

Nuclear reaction approaches such as Hauser-Feshbach [4] can give an accurate description of the neutron-capture cross section. However, the Hauser-Feshbach model requires accurate knowledge of the density of states up to the neutron-decay threshold. A challenge in nuclear theory is to accurately compute the density of states. This is difficult because of the sheer number of levels and configurations and the strong nature of the nuclear Hamiltonian. One microscopic approach is to account for correlations at the Hartree-Fock level and to “count” noninteracting levels within the corresponding mean-field single-particle space [5]. Another is to use the shell-model Monte Carlo (SMMC) [6,7], which utilizes auxiliary fields to compute the thermal trace for the energy, from which, the density of states can be extracted from the inverse Laplace transform of the partition function [8]. A limitation of the SMMC is the sign problem, which primarily limits the approach to schematic interactions [7]. Moments methods, derived from random matrix theory and statistical spectroscopy, can be used to construct spin and

parity dependent level densities for realistic Hamiltonians [9–12]. Moment methods, however, have been limited by the ability to compute higher moments of the Hamiltonian, the overall structural form of the density of states, and must be matched to the exact energies for low-lying states. The stochastic estimation method [13] has a computational cost that is almost of the same order as the Lanczos method used here and requires a special computer code to apply the shifted Krylov-subspace method [14,15].

In this article, we report on a new framework to provide an accurate description of the statistical properties of a model Hamiltonian. Our specific application is the calculation of the nuclear density of states within the configuration-interaction approach using fully realistic nuclear Hamiltonians. From universal properties of the Lanczos algorithm, we will demonstrate that the first eight moments of the Hamiltonian can be obtained from just four Lanczos iterations, which, in turn, can provide an accurate description of the averaged, or global, properties of the nuclear system within the defined Hilbert space. Several procedures to extract the density of states for model Hamiltonians are presented here: (1) extrapolating the tridiagonal Lanczos matrix well beyond what is computationally viable, leading to an extrapolated Lanczos method (ELM) to efficiently compute the density of states within the configuration-interaction method; (2) an analytic continuation of the ELM method; and (3) an approximation of the level density based on the binomial distribution.

II. NUCLEAR STRUCTURE MODEL

The principal goal behind nuclear-structure models is to find energy eigenvalues and wave functions for the nuclear Hamiltonian within a well-defined Hilbert space. In the nuclear shell model [16], or configuration interaction, the Hilbert space is defined by a set of orbits, usually denoted by the principal quantum number n , orbital angular momentum l ,

*ormand1@llnl.gov

and angular momentum j . The nuclear wave functions are constructed through a set of basis states obtained by filling these orbits following the Pauli principle. The basis states can consist of a set of Slater determinants with well defined z -projection of angular momentum, $J_z = M$, in the so-called M -scheme, or by projecting angular momentum (and possibly isospin) onto the M -scheme Slater determinants. The N many-body basis states, $|\psi_i\rangle$, spanning the Hilbert space are used to construct the full solution, i.e., $|\Psi\rangle = \sum_i c_i |\psi_i\rangle$. The coefficients c_i are found by computing the matrix elements of the Hamiltonian, $H_{ij} = \langle \psi_i | \hat{H} | \psi_j \rangle$, and diagonalizing the resulting Hermitian matrix. One of the most effective methods to find the lowest eigenvalues is the Lanczos algorithm [17], which starts with an arbitrary vector $|v_1\rangle$ in the Hilbert space, and through successive operations of \hat{H} , the matrix \mathbf{H} is transformed into tridiagonal form. The first three terms are

$$\begin{aligned}\hat{H}|v_1\rangle &= \alpha_1|v_1\rangle + \beta_1|v_2\rangle, \\ \hat{H}|v_2\rangle &= \beta_1|v_1\rangle + \alpha_2|v_2\rangle + \beta_2|v_3\rangle, \\ \hat{H}|v_3\rangle &= \beta_2|v_2\rangle + \alpha_3|v_3\rangle + \beta_3|v_4\rangle,\end{aligned}\quad (1)$$

and the $|v_i\rangle$ form an orthonormal set. In practice this amounts to applying \hat{H} to the Lanczos vectors, and extracting the matrix elements through subsequent dot-product operations and reorthogonalization, e.g., $\alpha_1 = \langle v_1 | \hat{H} | v_1 \rangle$, and $\beta_1^2 = \langle v_1 | (\hat{H}^\dagger - \alpha_1)(\hat{H} - \alpha_1) | v_1 \rangle$ (note that the phase of any of the β_i is arbitrary). The power of the Lanczos algorithm is that following successive applications of \hat{H} (iterations), the eigenvalues of the tridiagonal matrix quickly converge to the extreme eigenvalues of the full matrix. Typically, the lowest energy in the model space, E_0 , is obtained in approximately 30 iterations regardless the matrix dimension.

Of particular interest is the behavior of the tridiagonal matrix elements with increasing iterations. After several iterations, the diagonal elements, α_i , are roughly constant and nearly equal to the first moment $H_1 = \frac{1}{N} \text{Tr}[\hat{H}] = \frac{1}{N} \sum_i H_{ii}$. At the same time, the off-diagonal elements, β_i , generally decrease to zero as $i \rightarrow N$, and exhibit a Gaussian-like behavior [18].

In this work, we will examine the level density for selected Cr, Fe, and Ge isotopes within the framework of the nuclear shell model. All shell-model calculations were performed using angular momentum projected basis states with the NuShellX shell-model code [19] framework. For the Fe isotopes, the model space is comprised of the $0f_{7/2}$, $0f_{5/2}$, $1p_{3/2}$, and $1p_{1/2}$ orbitals and the Hamiltonian is defined by the one- and two-body matrix elements of the GXPF1A interaction of Ref. [20]. The model space for the Ge isotopes consists of the $0f_{5/2}$, $1p_{3/2}$, $1p_{1/2}$, $0g_{9/2}$ orbitals. For the Ge isotopes, we present results for two different empirical Hamiltonians: (1) $j44b$ defined in the Appendix of Ref. [21] and (2) jun45 of Ref. [22]. Note that there are no spurious center-of-mass excitations in either of these model spaces.

III. COMPUTING THE HAMILTONIAN MOMENTS WITH LANCZOS

At its core, the Lanczos algorithm is a really moment method [23]; efficiently computing $2n$ moments of \hat{H} with

respect to the initial pivot vector $|v_1\rangle$ after n iterations. With the choice of $|v_1\rangle = \frac{1}{\sqrt{N}} \sum_i \phi_i |\psi_i\rangle$, where ϕ_i is a random phase, we find it is possible to efficiently compute several moments of the Hamiltonian with just a few Lanczos iterations. This is illustrated by the first Lanczos matrix element α_1 given by

$$\alpha_1 = \frac{1}{N} \sum_i H_{ii} + \sum_{i \neq j} \frac{\phi_i \phi_j}{N} H_{ji} = H_1 + \sum_{i \neq j} \frac{\phi_i \phi_j}{N} H_{ji}. \quad (2)$$

The remainder in Eq. (2) is generally small due to cancellations caused by the random phases and a diminishing magnitude due to the large factor N in the denominator. Thus, for systems with large dimensions $\alpha_1 \approx H_1$. If needed, higher accuracy can be obtained by using different random initial pivots and averaging. A small remainder in Eq. (2) then suggests a strategy to compute even higher moments \hat{H} via

$$M_k = \frac{1}{N} \text{Tr}[(\hat{H} - H_1)^k] \approx \langle v_1 | (\hat{H} - \alpha_1)^k | v_1 \rangle. \quad (3)$$

To compute the moments with Lanczos iterations, we note the recurrence relation for the n^{th} Lanczos vector

$$|v_n\rangle = \frac{\hat{h} - \alpha_{n-1} + \alpha_1}{\beta_{n-1}} |v_{n-1}\rangle - \frac{\beta_{n-2}}{\beta_{n-1}} |v_{n-2}\rangle, \quad (4)$$

with $\hat{h} = \hat{H} - \alpha_1$ and $|v_2\rangle = \frac{\hat{h}}{\beta_1} |v_1\rangle$. In the case that the remainder elements are small, we have the approximation $M_k \approx \langle v_1 | \hat{h}^k | v_1 \rangle$, which can be extracted from the Lanczos matrix elements through successive application of the recurrence relation, collecting powers of \hat{h} , and back substituting for previous moments. From the n th Lanczos iteration, which gives the Lanczos vectors up to v_{n+1} , the moment M_{n+1} can be obtained from the normalization condition $\langle v_{n+1} | v_{n+1} \rangle = 1$, while the moment M_n can be extracted from the orthogonality of the Lanczos vectors, i.e., $\langle v_n | v_{n+1} \rangle = 0$. For example, M_2 can be found from normalizing $|v_2\rangle$,

$$\langle v_2 | v_2 \rangle = \frac{\langle v_1 | \hat{h}^2 | v_1 \rangle}{\beta_1^2} = \frac{M_2}{\beta_1^2} = 1, \quad (5)$$

leading to

$$M_2 = \beta_1^2. \quad (6)$$

For M_3 , we use the orthogonality condition

$$\langle v_2 | v_3 \rangle = \frac{\langle v_2 | \hat{h} - (\alpha_2 - \alpha_1) | v_2 \rangle}{\beta_2} - \frac{\beta_1}{\beta_2} \langle v_2 | v_1 \rangle, \quad (7)$$

$$= \frac{\langle v_1 | \hat{h}[\hat{h} - (\alpha_2 - \alpha_1)] \hat{h} | v_1 \rangle}{\beta_2 \beta_1^2}, \quad (8)$$

$$= \frac{M_3}{\beta_2 \beta_1^2} - \frac{\alpha_2 - \alpha_1}{\beta_2} = 0, \quad (9)$$

giving

$$M_3 = \beta_1^2(-\alpha_1 + \alpha_2). \quad (10)$$

Overall, while the derivations are tedious, they are straightforward using the symbolic manipulation program

Mathematica. The first eight moments in terms of the matrix elements from the first four Lanczos iterations are given by

$$H_1 = \alpha_1, \quad (11)$$

$$M_2 = \beta_1^2, \quad (12)$$

$$M_3 = \beta_1^2(-\alpha_1 + \alpha_2), \quad (13)$$

$$M_4 = \beta_1^2(\alpha_1^2 - 2\alpha_1\alpha_2 + \alpha_2^2 + \beta_1^2 + \beta_2^2), \quad (14)$$

$$M_5 = \beta_1^2[-\alpha_1(3\alpha_2^2 + 2\beta_1^2 + 3\beta_2^2) + \alpha_3\beta_2^2 + 2\alpha_2(\beta_1^2 + \beta_2^2) - \alpha_1^3 + 3\alpha_2\alpha_1^2 + \alpha_2^3], \quad (15)$$

$$M_6 = \beta_1^2\{3\alpha_1^2(2\alpha_2^2 + \beta_1^2 + 2\beta_2^2) - 2\alpha_1[\alpha_2(3\beta_1^2 + 4\beta_2^2) + 2\alpha_3\beta_2^2 + 2\alpha_2^3] \\ + \alpha_3^2\beta_2^2 + 2\alpha_2\alpha_3\beta_2^2 + 3\alpha_2^2(\beta_1^2 + \beta_2^2) + \alpha_1^4 - 4\alpha_2\alpha_1^3 + \alpha_2^4 + \beta_1^4 + \beta_2^4 + 2\beta_1^2\beta_2^2 + \beta_2^2\beta_3^2\}, \quad (16)$$

$$M_7 = \beta_1^2\{-2\alpha_1^3(5\alpha_2^2 + 2\beta_1^2 + 5\beta_2^2) + 2\alpha_1^2[2\alpha_2(3\beta_1^2 + 5\beta_2^2) + 5\alpha_3\beta_2^2 + 5\alpha_2^3] \\ - \alpha_1[3\alpha_2^2(4\beta_1^2 + 5\beta_2^2) + 10\alpha_3\alpha_2\beta_2^2 + 5\beta_2^2(\alpha_3^2 + \beta_2^2 + \beta_3^2) + 5\alpha_2^4 + 3\beta_1^4 + 8\beta_1^2\beta_2^2] \\ 3\alpha_2^2\alpha_3\beta_2^2 + 4\alpha_2^2(\beta_1^2 + \beta_2^2) + \beta_2^2[2\alpha_3(\beta_1^2 + \beta_2^2 + \beta_3^2) + \alpha_4\beta_3^2 + \alpha_3^3] \\ + \alpha_2[\beta_2^2(2\alpha_3^2 + 3\beta_2^2 + 2\beta_3^2) + 3\beta_1^4 + 6\beta_2^2\beta_1^2] - \alpha_1^5 + 5\alpha_2\alpha_1^4 + \alpha_2^5\}, \quad (17)$$

$$M_8 = \beta_1^2\{5\alpha_1^4(3\alpha_2^2 + \beta_1^2 + 3\beta_2^2) - 20\alpha_1^3[\alpha_2(\beta_1^2 + 2\beta_2^2) + \alpha_3\beta_2^2 + \alpha_2^3] \\ + \alpha_1^2[15\alpha_2^2(2\beta_1^2 + 3\beta_2^2) + 30\alpha_3\alpha_2\beta_2^2 + 15\beta_2^2(\alpha_3^2 + \beta_2^2 + \beta_3^2) + 15\alpha_2^4 + 6\beta_1^4 + 20\beta_1^2\beta_2^2] \\ - 2\alpha_1(2\alpha_2^3(5\beta_1^2 + 6\beta_2^2) + 9\alpha_3\alpha_2^2\beta_2^2 + 3\alpha_2[\beta_2^2(2\alpha_3^2 + 3\beta_2^2 + 2\beta_3^2) + 2\beta_1^4 + 5\beta_2^2\beta_1^2] \\ + \beta_2^2\{ \alpha_3[5\beta_1^2 + 6(\beta_2^2 + \beta_3^2)] + 3\alpha_4\beta_3^2 + 3\alpha_3^3\} + 3\alpha_2^5) \\ + 3\alpha_3^2\beta_2^4 + \alpha_3^4\beta_2^2 + 2\alpha_3^2\beta_1^2\beta_2^2 + 4\alpha_2^3\alpha_3\beta_2^2 + 3\alpha_3^2\beta_2^2\beta_3^2 + \alpha_4^2\beta_2^2\beta_3^2 + 2\alpha_3\alpha_4\beta_2^2\beta_3^2 + 5\alpha_2^4(\beta_1^2 + \beta_2^2) \\ + 3\alpha_2^2[\beta_2^2(\alpha_3^2 + 2\beta_2^2 + \beta_3^2) + 2\beta_1^4 + 4\beta_2^2\beta_1^2] + 2\alpha_2\beta_2^2[\alpha_3(3\beta_1^2 + 3\beta_2^2 + 2\beta_3^2) + \alpha_4\beta_3^2 + \alpha_3^3] \\ + \alpha_1^6 - 6\alpha_2\alpha_1^5 + \alpha_2^6 + \beta_1^6 + \beta_2^6 + 3\beta_1^2\beta_2^4 + \beta_2^2\beta_3^4 + 3\beta_1^4\beta_2^2 + 2\beta_2^4\beta_3^2 + 2\beta_1^2\beta_2^2\beta_3^2 + \beta_2^2\beta_3^2\beta_4^2\}. \quad (18)$$

In addition, the scaled moments $R_k = M_k/\sigma^k$ (with $\sigma^2 = M_2 \approx \beta_1^2$) can easily be computed using these formulas with the substitutions $\alpha_i \rightarrow \alpha_i/|\beta_1|$ and $\beta_i \rightarrow \beta_i/|\beta_1|$.

The validity of Eqs. (11)–(18) is shown in Table I, where the moments extracted from the first four Lanczos (L) iterations from a single random pivot are compared with the exact (Ex) moments for several nuclei within the $1p0f$ -shell model space using the GXPF1A interaction [20]. These systems were chosen because they have large dimensions, $N \approx 2 - 4 \times 10^4$, but are still small enough to fully diagonalize. For M_{3-8} , we show the scaled moments $R_k = M_k/\sigma^k$. Overall, good agreement is obtained between the exact and Lanczos-inferred moments. Some differences exist, which tend to be larger for the higher moments, and are due to an imperfect cancellation in the remainder term that propagates further into the higher moments. We find, however, that the remainders in H_1 and M_2 decrease with increasing model space size. We find that these inferred moments are more than sufficient to describe the averaged properties of the Hamiltonian matrix and to model the average properties of the remaining Lanczos matrix elements.

In general, most systems within the $1p0f$ shell have been found to have $R_4 \approx 2.8$, $R_6 \approx 12$, and $R_8 \approx 65 - 75$. For the purpose of comparison, note that for a Gaussian distribution, $R_4 = 3$, $R_6 = 15$, and $R_8 = 105$.

As mentioned above, higher accuracy can be achieved by computing the moments stochastically; that is by using

N_{samp} different initial pivots $|v_1^j\rangle$ and averaging the resulting moments, i.e.,

$$M_k \approx \frac{1}{N_{\text{samp}}} \sum_j \langle v_1^j | \hat{h}^k | v_1^j \rangle. \quad (19)$$

The variance divided by the square root of the number of samples then provides an estimate of the error. This is shown in Fig. 1 for the $J^\pi = 0^+$ basis in ^{48}Cr for $N_{\text{samp}} = 10$ different initial random pivots (each sample is indicated by the black dots connected with the black line and labeled on the x axis by the index j) for H_1 , σ , and R_{3-8} . The solid blue line represents the running average for each moment, the dashed blue line shows the error in the averaging, and the solid red line is the exact result. The figure shows that for this relatively small system, any single initial pivot provides result with an accuracy of a few percent.

In Fig. 2, we show moments extracted for 10 different initial random pivots for the $J^\pi = 1/2^-$ states in ^{57}Fe . Again, the individual results are represented by the black points, while the solid and dashed blue lines represent the running average and the estimated error, respectively. We note that because of the large dimension of this system, $N = 13436903$, the variation in the individual samples is quite small; amounting to less than one percent. The exact results for H_1 and σ^2 , as computed with the computer code of Ref. [12], are shown with the red lines. Each of the initial pivots agree with H_1 to within 10 keV and σ to within 5 keV, and the averaged

TABLE I. Comparison between exact (Ex) moments and those computed with the first four Lanczos (L) iterations for selected nuclei in the $1p0f$ -shell model space using the GXPF1A interaction. H_1 is in units of MeV, M_2 is units of MeV^2 , while R_{3-8} are dimensionless.

	^{47}Cr $1/2^-$	^{47}Cr $3/2^-$	^{48}Cr 0^+	^{48}Cr 12^+	^{72}Kr 0^+	^{73}Kr $1/2^-$
H_1	Ex -46.326	-46.402	-55.004	-59.195	-363.738	-380.331
	L -46.335	-46.401	-54.996	-59.166	-363.695	-380.364
M_2	Ex 94.722	94.052	111.121	76.011	110.502	95.473
	L 94.766	93.284	111.828	75.645	110.853	97.063
R_3	Ex -0.067	-0.070	-0.072	-0.092	0.021	0.039
	L -0.089	-0.066	-0.067	-0.100	0.026	0.071
R_4	Ex 2.756	2.753	2.803	2.737	2.768	2.723
	L 2.763	2.780	2.777	2.765	2.763	2.710
R_5	Ex -0.612	-0.644	-0.685	-0.784	0.223	0.375
	L -0.711	-0.620	-0.703	-0.817	0.234	0.535
R_6	Ex 11.742	11.724	12.421	11.515	11.875	11.190
	L 11.700	11.866	12.387	11.894	11.817	11.331
R_7	Ex -5.359	-5.706	-6.505	-6.533	2.217	3.325
	L -5.436	-5.457	-7.776	-6.656	1.916	3.930
R_8	Ex 65.370	65.441	74.272	63.201	66.940	59.537
	L 63.491	65.525	77.997	67.283	66.255	61.830

moments are in excellent agreement with the exact result. This demonstrates that the Lanczos procedure to compute the moments improves with dimension.

In Figs. 3 and 4, the dependence on angular momentum [in particular, the square $J(J+1)$] of the first eight moments is shown for calculations of both ^{57}Fe and ^{74}Ge . The ^{74}Ge

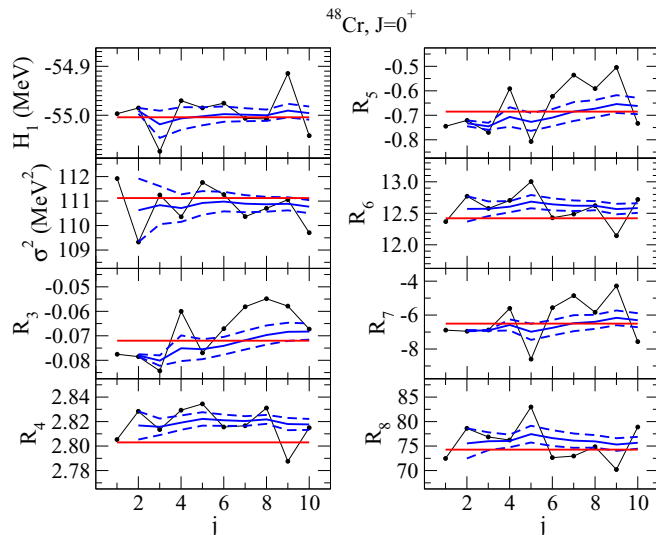


FIG. 1. Moments (H_1 , σ , and R_{3-8}) computed with 10 initial random pivots for the $J^\pi = 0^+$ basis in ^{48}Cr . The results for each initial vector v_i^j are indicated with the black dots connected with the black line and labeled on the x axis by j . The solid blue line represents the running average for each moment, the dashed blue shows the error in the averaging, and the solid red line is the exact result.

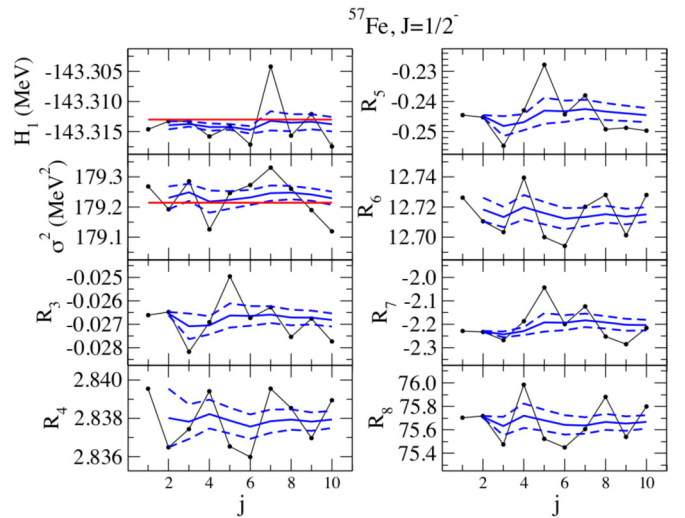


FIG. 2. Moments (H_1 , σ , and R_{3-8}) computed with 10 initial random pivots for the $J^\pi = 1/2^-$ basis in ^{57}Fe . The results for each initial vector v_i^j are indicated with the black dots connected with the black line and labeled on the x axis by j . The solid blue line represents the running average for each moment, the dashed blue shows the error in the averaging, and the solid red line is the exact result for H_1 and σ^2 .

results were obtained with the $jj44b$ interaction of Ref. [21]. A strong dependence on the square of the angular momentum is demonstrated for both the first and second moments for both nuclei. For ^{57}Fe , the scaled higher moments R_k exhibit a weak additional dependence on angular momentum. However, in ^{74}Ge , the higher scaled moments show a marked decrease with increasing angular momentum. Indeed, the eigenspectrum transitions to a more Gaussian-like distribution since R_8 decreases from a large value of 150 to 100. Also, we note that for low angular momenta $R_4 > 3$. Finally, the moments for the positive- and negative-parity spaces are nearly identical.

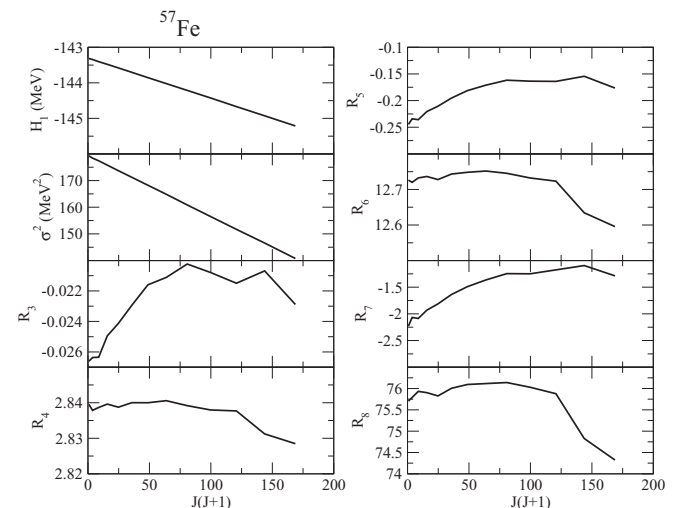


FIG. 3. The ^{57}Fe moments (H_1 , σ , and R_{3-8}) as a function of the square of the angular momentum $J(J+1)$.

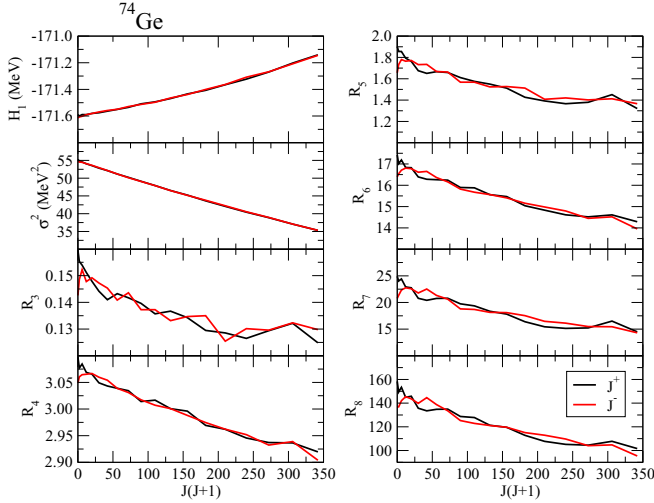


FIG. 4. The ^{74}Ge moments (H_1 , σ , and R_{3-8}) as a function of the square of the angular momentum $J(J+1)$. The black line shows the dependence for positive-parity states (J^+), while the red line shows the negative-parity states (J^-).

IV. MODELING THE LANCZOS MATRIX ELEMENTS

For large dimensions (e.g., $>10^8$), the computational effort for a shell-model calculation is determined by the Lanczos method; in particular the application of the Hamiltonian to the pivot vectors to generate the tridiagonal matrix. The resulting tridiagonal matrix with dimensions of 10^{1-3} can easily be diagonalized in a few seconds, while a tridiagonal matrix with a dimension of the order 10^5 can be diagonalized within a few minutes. Thus, our goal is to develop a method to model the entire tri-diagonal matrix based on the first eight moments. We propose the polynomial form defining the Lanczos matrix elements at each iteration i as

$$\alpha_i = a_0 + a_1 z_i + a_2 z_i^2 + a_3 z_i^3, \quad (20)$$

$$\beta_i^2 = b_1 z_i [1 + b_2 z_i + b_3 z_i^2 + b_4 z_i^3], \quad (21)$$

where $z_i = \ln(i/N)$. We note that this representation is different from the inverse binomial of Ref. [18] and the shifted Gaussian of Ref. [24]. This representation provides the flexibility to accurately model the Lanczos matrix elements for a wide range of systems including those where the scaled fourth moment is greater than the Gaussian limit, $R_4 > 3$, as is encountered with Ge isotopes. In addition, the large N limit leads to useful analytic formulas for the moments that can be useful to fix the parameters.

The a and b coefficients can be determined by requiring that the moments of the modeled matrix elements reproduce moments of the Hamiltonian. We note that while the moments are in general high-order polynomials in the a and b parameters, they are, themselves, most sensitive to the odd and even moments, respectively. Further, the dominant parameter is b_1 , which effectively determines the second moment M_2 . Also, a_0 is trivially constrained by H_1 since it does not affect any of the higher moments. Last, we note that many systems (although not all as, is observed later for ^{76}Ge) have nearly the same value for b_2 . This is due to the fact, as seen in Table I, that $R_4 \approx 2.7-2.8$, which is close to the Gaussian limit of 3.

The first eight moments of the tridiagonal matrix can be computed via

$$H_1 = \langle \alpha \rangle, \quad (22)$$

$$M_2 = \langle (\alpha - \langle \alpha \rangle)^2 \rangle + 2\langle \beta^2 \rangle, \quad (23)$$

$$M_3 \approx \langle (\alpha - \langle \alpha \rangle)^3 \rangle + 6\langle (\alpha - \langle \alpha \rangle)\beta^2 \rangle, \quad (24)$$

$$M_4 \approx \langle (\alpha - \langle \alpha \rangle)^4 \rangle + 12\langle (\alpha - \langle \alpha \rangle)^2 \beta^2 \rangle + 6\langle \beta^4 \rangle, \quad (25)$$

$$M_5 \approx \langle (\alpha - \langle \alpha \rangle)^5 \rangle + 20\langle (\alpha - \langle \alpha \rangle)^3 \beta^2 \rangle + 30\langle (\alpha - \langle \alpha \rangle)\beta^4 \rangle, \quad (26)$$

$$M_6 \approx \langle (\alpha - \langle \alpha \rangle)^6 \rangle + 30\langle (\alpha - \langle \alpha \rangle)^4 \beta^2 \rangle + 90\langle (\alpha - \langle \alpha \rangle)^2 \beta^4 \rangle + 20\langle \beta^6 \rangle, \quad (27)$$

$$M_7 \approx \langle (\alpha - \langle \alpha \rangle)^7 \rangle + 42\langle (\alpha - \langle \alpha \rangle)^5 \beta^2 \rangle + 210\langle (\alpha - \langle \alpha \rangle)^3 \beta^4 \rangle + 140\langle (\alpha - \langle \alpha \rangle)\beta^6 \rangle, \quad (28)$$

$$M_8 \approx \langle (\alpha - \langle \alpha \rangle)^8 \rangle + 56\langle (\alpha - \langle \alpha \rangle)^6 \beta^2 \rangle + 420\langle (\alpha - \langle \alpha \rangle)^4 \beta^4 \rangle + 560\langle (\alpha - \langle \alpha \rangle)^2 \beta^6 \rangle + 70\langle \beta^8 \rangle, \quad (29)$$

where $\langle \dots \rangle \rightarrow \frac{1}{N} \sum_j \dots$, which for large N can be extended to the integral $\frac{1}{N} \int_1^N \dots dx$. The approximate equality arises from the assumption that adjacent matrix elements β_i , $\beta_{i\pm 1}$, $\beta_{i\pm 2}$, $\beta_{i\pm 3}$ are nearly equal. With Eqs. (22)–(29) the a and b parameters can be “fit” to reproduce the moments of the Hamiltonian, leading to a modeled tridiagonal matrix with the same moments as the original Hamiltonian.

In principle, analytic formulas can be obtained for the moments in the large N limit since

$$\lim_{N \rightarrow \infty} \int_1^N \ln^m x dx = m!. \quad (30)$$

In this limit, the first five moments as defined in Eqs. (22)–(26) are given in terms of the a and b parameters of Eqs. (20) and (21) by

$$H_1 = a_0 - a_1 + 2a_2 - 6a_3, \quad (31)$$

$$M_2 = a_1^2 + (36a_3 - 8a_2)a_1 + 4(5a_2^2 - 54a_3a_2 + 171a_3^2) + 2b_1(2b_2 - 6b_3 + 24b_4 - 1) \quad (32)$$

$$M_3 = -2[a_1^3 - 18(a_2 - 6a_3)a_1^2 + 12(10a_2^2 - 135a_3a_2 + 513a_3^2)a_1 - 8(37a_2^3 - 837a_3a_2^2 + 7047a_3^2a_2 - 21897a_3^3)] + 6b_1[18a_3(-6b_2 + 38b_3 - 272b_4 + 1) + a_1(-4b_2 + 18b_3 - 96b_4 + 1) + 4a_2(5b_2 - 27b_3 + 168b_4 - 1)], \quad (33)$$

$$\begin{aligned}
M_4 = & 3[3a_1^4 + (552a_3 - 80a_2)a_1^3 + 8(113a_2^2 - 1746a_3a_2 + 7515a_3^2)a_1^2 - 32(158a_2^3 - 4059a_3a_2^2 + 38412a_3^2a_2 - 132921a_3^3)a_1 \\
& + 16(731a_2^4 - 27540a_3a_2^3 + 427014a_3^2a_2^2 - 3208572a_3^3a_2 + 9800919a_3^4)] + 12b_1\{a_1^2(14b_2 - 78b_3 + 504b_4 - 3) \\
& - 4a_1[a_2(44b_2 - 282b_3 + 2064b_4 - 8) - 9a_3(32b_2 - 234b_3 + 1928b_4 - 5)] + 4[a_2^2(158b_2 - 1146b_3 + 9384b_4 - 25) \\
& - 36a_3a_2(65b_2 - 531b_3 + 4844b_4 - 9) + 9a_3^2(1082b_2 - 9846b_3 + 99144b_4 - 133)]\} \\
& + 12b_1^2[12b_2^2 - 6(20b_3 - 120b_4 + 1)b_2 + 360b_3^2 + 20160b_4^2 + b_3(24 - 5040b_4) - 120b_4 + 1], \quad (34)
\end{aligned}$$

$$\begin{aligned}
M_5 = & -4[11a_1^5 + 10(43a_2 - 342a_3)a_1^4 - 20(371a_2^2 - 6507a_3a_2 + 31410a_3^2)a_1^3 \\
& + 40(1756a_2^3 - 50625a_3a_2^2 + 532332a_3^2a_2 - 2029563a_3^3)a_1^2 \\
& - 80(4534a_2^4 - 189909a_3a_2^3 + 3245859a_3^2a_2^2 - 26685153a_3^3a_2 + 88602417a_3^4)a_1 \\
& + 32(25411a_2^5 - 1442205a_3a_2^4 + 35446860a_3^2a_2^3 - 469283490a_3^3a_2^2 + 3331562805a_3^4a_2 - 10104948693a_3^5)] \\
& + 20b_1\{a_1^3(-64b_2 + 426b_3 - 3216b_4 + 11) \\
& + 6a_1^2[2a_2(119b_2 - 891b_3 + 7488b_4 - 18) - 9a_3(202b_2 - 1694b_3 + 15792b_4 - 27)] \\
& - 12a_1[a_2^2(988b_2 - 8238b_3 + 76416b_4 - 133) - 36a_3a_2(466b_2 - 4313b_3 + 44036b_4 - 56) \\
& + 9a_3^2(8764b_2 - 89298b_3 + 996336b_4 - 949)] \\
& + 8[a_2^3(4534b_2 - 41754b_3 + 424416b_4 - 548) - 27a_3a_2^2(4714b_2 - 47818b_3 + 531392b_4 - 513) \\
& + 54a_3^2a_2(24245b_2 - 268947b_3 + 3246768b_4 - 2395) + 27a_3^3(-181498b_2 + 2187714b_3 - 28528896b_4 + 16391)]\} \\
& - 120b_1^2\{-a_2[168b_2^2 - 6(400b_3 - 3240b_4 + 9)b_2 + 9720b_3^2 + 887040b_4^2 - 2400b_4 - 336b_3(525b_4 - 1) + 5] \\
& + a_1[24b_2^2 - 3(100b_3 - 720b_4 + 3)b_2 + 1080b_3^2 + 80640b_4^2 - 300b_4 - 24b_3(735b_4 - 2) + 1] \\
& + 9a_3[136b_2^2 - 2(1100b_3 - 9960b_4 + 19)b_2 + 9960b_3^2 + 1102080b_4^2 - 2200b_4 - 272b_3(735b_4 - 1) + 3]\}. \quad (35)
\end{aligned}$$

For $k > 5$, these formulas are more complicated with extremely large coefficients. Nonetheless, the analytic formulas for M_3 and M_5 are useful for providing initial estimates for the parameters a_1 and a_2 . An alternative, that is somewhat more efficient for the higher moments ($k \geq 5$), and was used here to determine the parameters, is to evaluate the moment integrals numerically using z as the integration variable, which involves integrals of the form

$$\frac{1}{N} \int_{\ln(1/N)}^0 e^z z^m dz. \quad (36)$$

Sufficient accuracy can be achieved using Simpson's rule with 10^5 points. For numerical stability, the integrals can be evaluated by scaling relative to M_2 by taking $a_i \rightarrow a_i/\sqrt{-b_1}$ followed by setting $b_1 \rightarrow -1$.

The procedure used here to find the a and b parameters is discussed in Appendix A.

The utility of the moment method to describe the nuclear Hamiltonian is illustrated in Fig. 5 where the modeled (colored lines) Lanczos matrix elements are compared with those obtained from a shell-model calculation (black lines) for the ^{48}Cr , $J^\pi = 0^+$ (top) and ^{57}Fe , $J^\pi = 25/2^-$ (bottom) systems. For ^{48}Cr , the entire Lanczos matrix ($N = 41355$) is plotted, while for ^{57}Fe , $J^\pi = 25/2^-$ ($N = 13752093$), 3074 Lanczos iterations were performed and 100000 modeled matrix elements are shown. The ^{48}Cr system is somewhat typical where the dominant behavior observed in the Lanczos matrix can be extracted from just the first four moments, i.e., M_3

to constrain a_1 and M_2 and M_4 to constrain b_2 and b_4 . Still, the figure shows that using moments up to M_8 can improve the overall description of modeled Lanczos matrix. The ^{57}Fe system is different in that the higher moments are essential. The figure shows that limiting to M_3 to constrain a_1 is clearly inadequate and improvement is achieved only by including the higher odd moments, and the best overall results are obtained using all eight moments. The ^{57}Fe case is also interesting as it has a negative skewness (M_3), which is correctly captured with the Lanczos method to compute the moments, but also seemingly contradicts the positive values of $(\alpha_i - H_1)$ shown for the first few thousand iterations. Indeed, the diagonal matrix elements show a strong curvature and eventually turn negative for large iteration number. This is captured in the higher odd moments leading to quadratic and cubic terms in the modeled α_i matrix elements. Last, the β_i at low iteration number are also influenced by the higher even moment M_6 .

V. ESTIMATING THE LEVEL DENSITY

The density of states is a key nuclear property that has a significant impact on reaction rates for statistical processes, such as radiative neutron capture. For the most part, reaction models, such as Hauser-Feshbach [4], have relied on a parametrization of the level density based on a modified back-shifted Fermi gas approach such as was introduced by Gilbert and Cameron [25]. This approach requires knowledge about

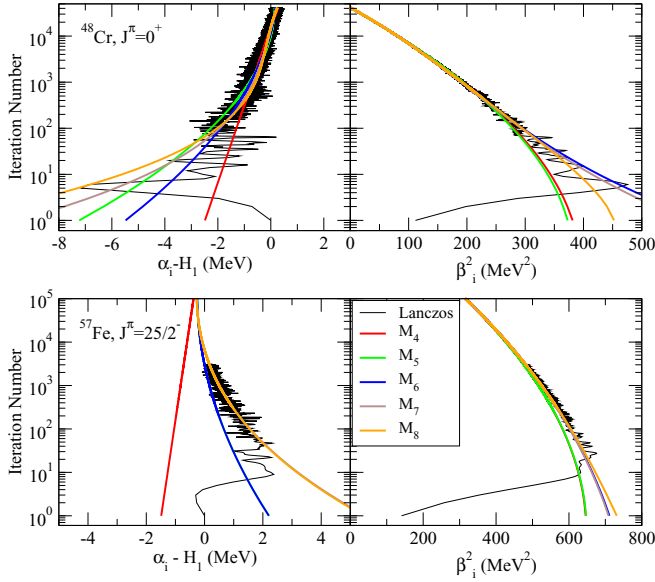


FIG. 5. Comparison between shell model (black) and modeled Lanczos matrix elements α and β for ^{48}Cr , $J^\pi = 0^+$ (top) and ^{57}Fe , $J^\pi = 25/2^-$ (bottom) within the $1p0f$ -model space using the GXPF1A interaction [20]. The colored curves show modeled Lanczos matrix elements using Eqs. (20) and (21) with the indicated moments to constrain the a and b parameters.

several parameters such as the single-particle level-density parameter a , which may depend on excitation energy, the pairing gap Δ , and the spin cutoff parameter. In addition, the back-shifted Fermi gas density is matched to the low-lying spectrum where the level density is assumed to follow an exponential form. The matching is accomplished by requiring that the exponential component reproduces the cumulative density up to an excitation where the discrete levels are both known and complete and requiring continuity in the logarithmic derivative of the level density (equivalent to the inverse temperature) at the matching energy. A drawback of this procedure is that the level-density parameters are generally constrained by experimental knowledge, such as the spacings of $l = 0$ (D_0) and $l = 1$ (D_1) resonances at the neutron separation energy, S_n . These quantity are generally known only in systems based on a stable target. For radiative neutron capture, the level density is needed essentially up to the neutron separation energy.

One approach to generalize our knowledge of the level density is to use theoretical structure models based on the microscopic physics involved, such as the nuclear shell model, where high-quality empirical nuclear Hamiltonians have been developed that are well-known to reproduce the low-lying spectra of nuclei. It is important to note that these shell-model calculations are based on a finite model space, and at some excitation energy, E_x , they will fail to adequately enumerate the system due to the presence of so-called “intruder” states. These intruder states, however, are expected to occur at higher excitation energies, generally of the order of the shell gap for states with opposite parity and twice the shell gap for states of the same parity. Thus, in many cases it is not unreasonable

to hope that a large-basis shell-model calculation contains sufficient configurations to adequately describe the states of a given parity up to excitation energies near the neutron separation energy. This supposition can be tested in a few cases through comparison with experimentally measured resonance spacings. For example, within the $1p0f$ -shell, the calculated density of states can be compared with the $l = 1$ spacings D_1 , at which point, the computed level density can be used to define parameters of the back-shifted Fermi gas needed to describe the full level density.

The most straight forward approach to compute the density of states within the shell model would be to simply diagonalize the model Hamiltonian and count the respective states. In many cases, this is computationally prohibitive since the number of the configurations within the model space can exceed 10^9 . Instead, since the density of states is more of a statistical property of the Hamiltonian, we propose to model the Hamiltonian via the moments method outlined above and to compute the density of states from the modeled matrix. Another approach would be to use the binomial distribution described in Ref. [18], which is constrained with just the first four moments of the Hamiltonian and is appealing due to its analytic nature. In what follows, several approaches to determine the density of states as a function of excitation energy are outlined.

A. Extrapolated Lanczos method

Section IV illustrated that for most cases the global, or averaged, properties of the Lanczos matrix can be predicted from just four Lanczos iterations. This offers a strategy to predict the statistical properties of the entire energy spectrum by performing a set of Lanczos iterations sufficient to describe the low-lying spectrum and then extrapolate the Lanczos matrix elements with Eqs. (20) and (21) to an iteration number sufficient to properly estimate the density of states. We refer to this as $\text{ELM}(k, N_{\text{Lanc}})$, where k denotes the maximum moment M_k used to extrapolate the Lanczos matrix elements and N_{Lanc} is the number of actual Lanczos iterations used prior to extrapolation. In general, the Lanczos iterations can be computationally expensive for large model spaces, and a key question is just what value of N_{Lanc} is sufficient and/or optimal. A general requirement is obtaining sufficient accuracy in the ground-state energy, E_{gs} , to establish the excitation energy scale to measure the density of states. The accuracy required in E_{gs} is model space and Hamiltonian dependent. For example, for the model spaces and Hamiltonians studied in this work, we found that an uncertainty of 10 keV in E_{gs} leads to a 1% uncertainty in the level density, while a 100 keV uncertainty leads to a 10% change in the level density. As a general rule, 30–40 Lanczos iterations are needed to determine the ground-state energy with an accuracy better than 10 keV, and more often than not, with an accuracy of 1 keV. To some degree, an optimal number of Lanczos iterations can be thought of as where a smooth transition (within the fluctuations of the Lanczos matrix elements) occurs between the computed and modeled Lanczos matrix elements. This may not always be practical, and while it is true that too few iterations can lead to difficulties in the direct computation

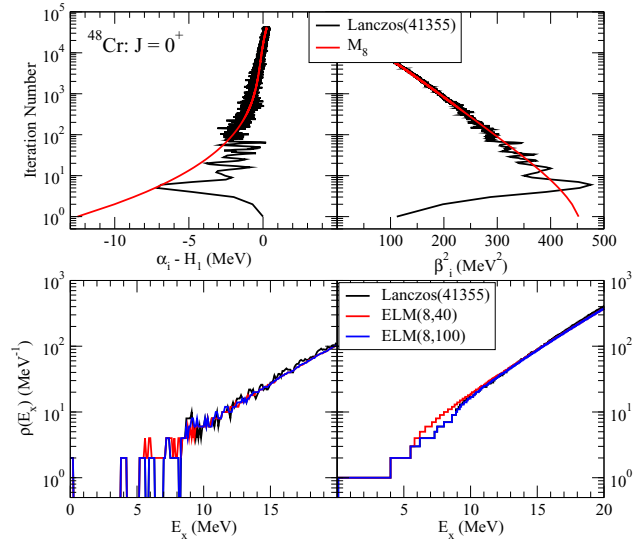


FIG. 6. Results for the $J^\pi = 0^+$ space in ^{48}Cr within the $1p0f$ -shell model space with the GXPF1A interaction. The black lines show the shell-model calculations for the Lanczos matrix elements in the upper half of the figure and the level density and cumulative level density in the bottom obtained with 41355 Lanczos iterations. In the lower half of the figure, the level density and cumulative density are shown for ELM(8,40) (red) and ELM(8,100) (blue).

of the level density at lower excitation energies, an analytic continuation method, discussed below, can address this issue. Consequently, it is often possible to achieve excellent results with the ELM method with N_{Lanc} as low as 40.

In Fig. 6, results for the $J^\pi = 0^+$ space in ^{48}Cr are shown. The shell model calculation was performed using the GXPF1A interaction [20] within the $1p0f$ -shell model space with the shell model-code NuShell. Here, the full shell-model matrix was diagonalized with the Lanczos algorithm. The black lines show the results from the shell-model calculation obtained with $N_{\text{Lanc}} = 41355$ Lanczos iterations. The Lanczos matrix elements are displayed in the top half of the figure and the level density and cumulative density shown in the left and right sides, respectively, in the bottom half of the figure. In this, and subsequent figures, the actual Lanczos results are labeled as Lanczos(N_{Lanc}), with N_{Lanc} being the number of iterations performed. The level density was computed as a function of excitation energy in steps of 100 keV as a running average within an energy window of $E_x \pm 500$ keV, which smooths out fluctuations in the level density. The red and blue lines show the results for ELM(8,40) and ELM(8,100), respectively. The Lanczos matrix was then extrapolated to the full dimension of the system (41355) using the modeled α and β matrix elements of Eqs. (20) and (21) constrained with the moments of the actual shell-model Hamiltonian. In this case, all 41355 eigenvalues were used to compute the level density. The ground-state energy for each calculation was computed from the shell-model Lanczos matrix elements with the N_{Lanc} elements. The ELM(8,100) calculation is nearly indistinguishable from the shell model calculation. The ELM(8,40) calculation shows a slight deviation from the exact shell model calculation at $E_x \approx 6$ MeV. This deviation

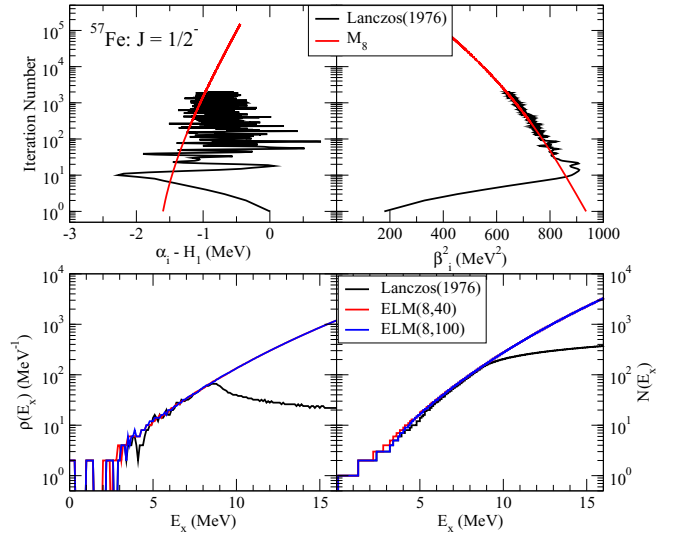


FIG. 7. Results for the $J^\pi = 1/2^-$ space in ^{57}Fe within the $1p0f$ -shell model space with the GXPF1A interaction. The black lines show the shell-model calculations for the Lanczos matrix elements in the upper half of the figure and the level density and cumulative level density in the bottom obtained with 1976 Lanczos iterations. In the lower half of the figure, the level density and cumulative density are shown for ELM(8,40) (red) and ELM(8,100) (blue).

is primarily due to a small discontinuity in the matching of the Lanczos matrix elements at N_{Lanc} and hints at how the ELM(k, N_{Lanc}) approach can break down.

In addition to the demonstration for ^{48}Cr , we have also applied and tested the ELM method to ^{57}Fe for $J^\pi = 1/2^- - 25/2^-$ and ^{76}Ge for $J = 0^\pm - 14^\pm$. In what follows, representative results for these systems are shown to demonstrate various features of the ELM method. We note that applications of the ELM(2,100) method to the Fe region were published earlier in Ref. [26].

Shown in Figs. 7 and 8 are the results obtained for the $1/2^-$ and $25/2^-$ states in ^{57}Fe , while the moments are given in Table II. Again, the solid black lines are the results for the shell-model calculation, while the red and blue lines represent the ELM(8,40) and ELM(8,100) results, respectively. The

TABLE II. Comparison of moments computed with the first four Lanczos iterations for the $1/2^-$ and $25/2^-$ angular momentum configuration space in ^{57}Fe . H_1 is in units of MeV, M_2 is units of MeV^2 , while R_{3-8} are dimensionless.

	^{57}Fe $1/2^-$	^{57}Fe $25/2^-$
H_1	-143.314	-145.213
M_2	179.268	140.764
R_3	-0.026	-0.022
R_4	2.839	2.828
R_5	-0.244	-0.176
R_6	12.726	12.595
R_7	-2.229	-1.287
R_8	75.703	74.324

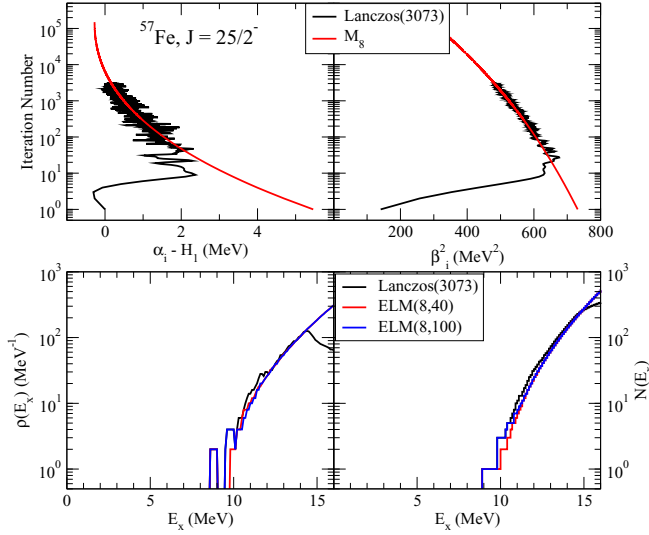


FIG. 8. Results for the $J^\pi = 25/2^-$ space in ^{57}Fe within the $1p0f$ shell-model space with the GXPFI1A interaction. The black lines show the shell-model calculations for the Lanczos matrix elements in the upper half of the figure and the level density and cumulative level density in the bottom obtained with 3073 Lanczos iterations. In the lower half of the figure, the level density and cumulative density are shown for ELM(8,40) (red) and ELM(8,100) (blue).

level densities were computed by extrapolating the the Lanczos matrix elements to 150 000 iterations, diagonalizing the resulting matrix, and as a running average over an excitation energy window of $E_x \pm 500$ keV. The primary difference between the $1/2^-$ and $25/2^-$ angular momentum spaces lies with the odd moments. Both systems have nearly identical negative skewness (R_3) as is shown in Table II. The high-spin state, however, has a large nonlinear term, and the $(\alpha_i - H_1)$ are actually positive for smaller iteration number, and then decrease and become negative at large iteration number. A signature of this behavior is also exhibited in the higher odd moments. In particular, when M_3 dominates the spectral behavior (linear terms in the α_i), one often finds $R_7 \sim 9.0-9.5R_5$ and $R_5 \sim 9.0-9.5R_3$. Instead, for the $25/2^-$ space $R_7 \sim 7.3R_5$ and $R_5 \sim 8R_3$.

This section, demonstrating the ELM approach, is concluded with an examination of the $J^\pi = 0^+$ and 4^+ systems in ^{76}Ge using the $jj44b$ interaction of Ref. [21]. The computed moments are shown in Table III. The key features of this system are: (1) the large skewness ($R_3 \sim 0.2$), which is an order of magnitude larger than that observed in ^{57}Fe , (2) the large fourth moment ($R_4 > 3$, which is substantially larger than the Gaussian value of 3), and (3) the dramatic difference in the 8th moment between the two angular momenta.

Shown in Figs. 9 and 10 are the results for 0^+ and 4^+ states, respectively, for ^{76}Ge obtained with the $jj44b$ interaction. The level density was computed by extrapolating the Lanczos matrix to a dimension of 150 000, diagonalizing the resulting tridiagonal matrix, and computing a running average within the excitation energy window of $E_x \pm 500$ keV. For illustrative purposes, approximately 1000 lanczos iterations were

TABLE III. Comparison of moments computed with the first four Lanczos iterations for 0^+ and 4^+ states in ^{76}Ge . H_1 is in units of MeV, M_2 is units of MeV^2 , while R_{3-8} are dimensionless.

	^{76}Ge 0^+	^{76}Ge 4^+
H_1	-190.500	-190.544
M_2	47.911	46.021
R_3	0.228	0.201
R_4	3.266	3.135
R_5	3.079	2.441
R_6	22.298	18.436
R_7	53.417	32.914
R_8	310.668	180.656

performed in each space to diagnose the calculation of the level density. The results for the $J^\pi = 0^+$ space are similar to those shown earlier for ^{48}Cr and ^{57}Fe where the ELM(8,100) closely matches the shell-model result. This is not the case, however, for the $J^\pi = 4^+$ where there is a clear discrepancy in the spectrum at $E_x \approx 3-5$ MeV. However, the ELM(8, N_{Lanc}) results agree with the shell model at higher excitation energies, as would be expected since this is the regime where the statistical nature of the configuration space should dominate the spectral behavior. The cause of this discrepancy is evident in the upper part of the figure where the diagonal α_i matrix elements exhibit a clear transition in their behavior. The figure shows that the modeled matrix elements capture the overall behavior of the Lanczos matrix elements for large iteration number, but fail to describe the “step” behavior shown to at approximately 400 iterations. Thus, the modeled

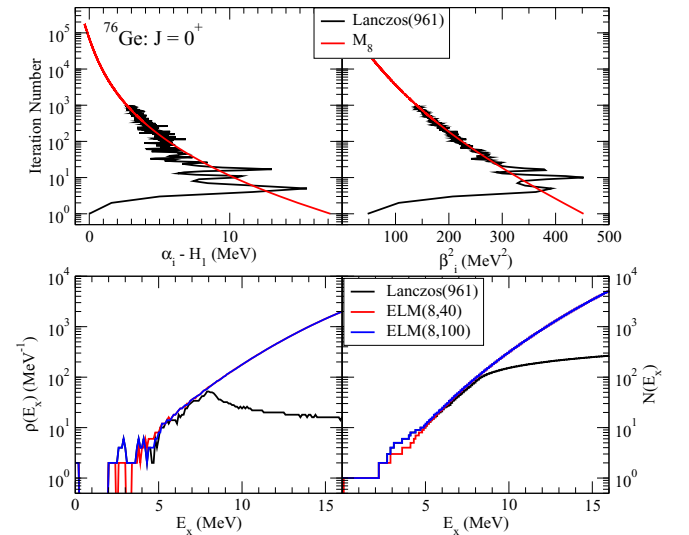


FIG. 9. Results for the $J^\pi = 0^+$ space in ^{76}Ge within the $jj44b$ shell-model space with the $jj44b$ interaction. The black lines show the shell-model calculations for the Lanczos matrix elements in the upper half of the figure and the level density and cumulative level density in the bottom obtained with 961 Lanczos iterations. In the lower half of the figure, the level density and cumulative density are shown for ELM(8,40) (red) and ELM(8,100) (blue).

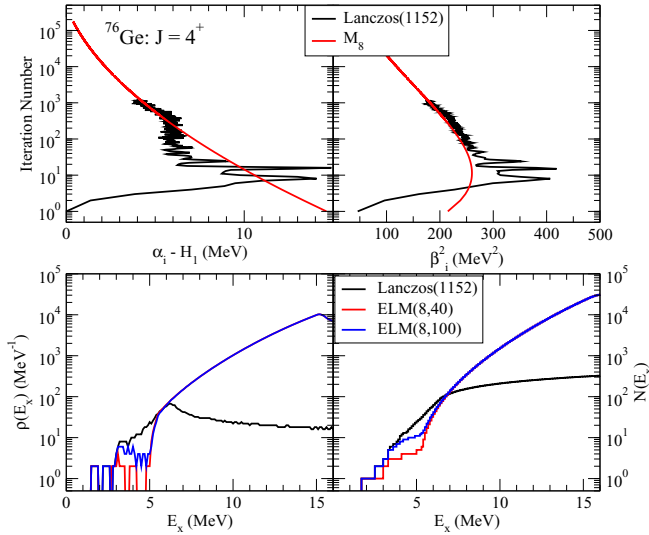


FIG. 10. Results for the $J^\pi = 4^+$ space in ^{76}Ge within the $jj44$ shell-model space with the $jj44b$ interaction. The black lines show the shell-model calculations for the Lanczos matrix elements in the upper half of the figure and the level density and cumulative level density in the bottom obtained with 1152 Lanczos iterations. In the lower half of the figure, the level density and cumulative density are shown for ELM(8,40) (red) and ELM(8,100) (blue).

matrix elements lead to a strong dip in the level density for $E_x \approx 3\text{--}5$ MeV that is caused by a strong discontinuity between the modeled and actual matrix elements that is far larger than scatter, or noise, exhibited in the computed Lanczos matrix elements. In this case, it would be necessary to perform an ELM(8,400) calculation to more accurately describe the system. It has to be noted that often times such a calculation can be computationally prohibitive. In addition, while these calculations for ^{76}Ge are quite different than those in the $1p0f$ shell, it is not always clear if, or where, a sudden transition in the computed matrix elements may take place; especially for model spaces involving orbits in different major shells. As is apparent from the upper part of Fig. 10, the clearest signature of a potential problem with the ELM procedure is the existence of a strong discontinuity at N_{Lanc} between the compute Lanczos matrix elements and the modeled matrix elements. This discontinuity may be present in either the α_i matrix elements, the β_i matrix elements, or both. If such a discontinuity exists, then two alternatives are suggested: (1) an alternative extrapolation that smoothly joins the computed and modeled matrix elements to within the “noise” in the matrix elements, or (2) a procedure to analytically continue the level density from the high-energy regime to the lowest state in the model space. The latter approach will be discussed in Sec. V C.

Here, we recap the primary features of the ELM. A general first requirement is to compute the ground-state energy of the system with an accuracy of 10 keV or better, which can generally be achieved for any Hamiltonian and configuration space with approximately 40 iterations. From the first four Lanczos iterations, the lowest 8 moments of the Hamiltonian can be computed, which can then be used to model the diago-

nal, α_i , and off diagonal, β_i , Lanczos matrix elements. Using Eqs. (20) and (21), the Lanczos matrix can be extrapolated (or modeled) to any desired dimension, N_{extrap} . The energy eigenvalues of this extrapolated matrix provide a reasonable description of the energy eigenvalues that would be obtained from shell model system if N_{extrap} actual Lanczos iterations had been performed. The value of N_{extrap} is dependent on the dimension of the shell model system and the maximum energy that is desired for the level density. For the most part, due to the finite model space, i.e., the finite number of single-particle orbitals included, the maximum energy that we should reasonably expect to be able to model the level density with the shell model is of the order 10 MeV. A general feature of the Lanczos procedure is that the extremal eigenvalues converge first and exhibit a density commiserate with the actual level density. However, the eigenvalues in the middle of the spectrum are slow to converge and tend to be fairly equally spaced. This behavior is nicely exhibited in Figs. 7–10 for the actual Lanczos calculations. For example, the black curve labeled Lanczos(1937) in the bottom left part of Fig. 7 increases steadily up to an energy of $\approx 8\text{--}9$ MeV and then abruptly decreases and flattens out across the middle of the spectrum. This a universal feature of the Lanczos procedure for a finite number of iterations, and the extrapolated iteration number, N_{extrap} , needs to be chosen large enough so that the sharp decline in the level density occurs above the region of interest. Computationally, finding the eigenvalues of a tridiagonal matrix with dimension 200 000 takes of the order 5–10 min, which is orders of magnitude faster than the time required to perform the same number of actual Lanczos iterations.

B. Binomial approximation for the level density

In Ref. [10], a binomial form was proposed to describe the density of states for quantum many-body systems, such as those described by the nuclear shell model. For a system of dimension \mathcal{N} , three parameters are required to define the binomial: \mathcal{N} the effective dimension of the system, the asymmetry p , and an energy scale ϵ . The span S (the energy difference between the lowest and highest states), centroid E_c , variance σ^2 , and dimensionless energy x are given by

$$S = \mathcal{N}\epsilon, \quad E_c = \mathcal{N}p\epsilon, \quad \sigma^2 = \mathcal{N}pq\epsilon^2, \quad x = \frac{E}{S}, \quad (37)$$

where $p + q = 1$ and obviously $E_c = H_1$ and $\sigma^2 = M_2$. The binomial approximation to the level density is then given by

$$\rho_b(x) = p^{x\mathcal{N}} q^{\bar{x}\mathcal{N}} \frac{\Gamma(\mathcal{N} + 1)}{\Gamma(x\mathcal{N} + 1)\Gamma(\bar{x}\mathcal{N} + 1)} \frac{\mathcal{N}\mathcal{N}}{S}, \quad (38)$$

with $\bar{x} = 1 - x$. The binomial parameters p and \mathcal{N} can be determined by the third and fourth moments of the Hamiltonian since for the binomial

$$R_3 = \frac{q - p}{\sqrt{\mathcal{N}pq}} \quad (39)$$

and

$$R_4 = 3 + \frac{1 - 6pq}{\mathcal{N}pq}. \quad (40)$$

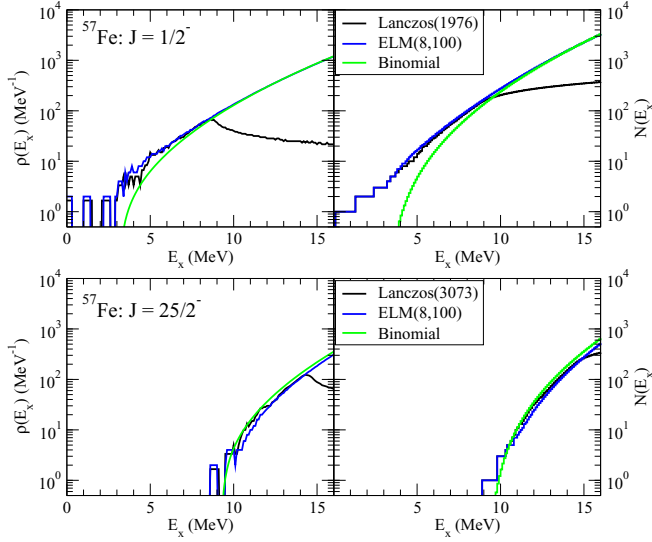


FIG. 11. Results for the level density and cumulative density for $J^\pi = 1/2^-$ and $25/2^-$ states in ^{57}Fe within the $1p0f$ shell-model space with the GXPF1A interaction. The black lines show the shell-model calculation, while the blue and green lines represent ELM(8,100) and the binomial approximation, respectively.

Defining $R = R_3^2/(R_4 - 3)$, the parameter p becomes

$$p = \frac{1}{2} \left[1 - \text{sgn}(M_3) \sqrt{1 - 2 \left(\frac{1 - R}{2 - 3R} \right)} \right], \quad (41)$$

from which, \mathcal{N} follows directly from Eq. (40). With p and \mathcal{N} known, the span is then given by

$$S = \sqrt{\frac{\mathcal{N}\sigma^2}{pq}}. \quad (42)$$

In addition, for the binomial, the ground-state energy is $E_{\text{gs}}^b = -Sp$, which may not correspond to the actual ground state energy E_{gs} . In this case, the level density in Eq. (38) is shifted by $x - (E_c - Sp)/S$ so that the binomial centroid corresponds to the centroid of the Hamiltonian relative to the exact ground state. For the most part, the most significant hurdle in implementing this approach has been the ability to compute R_3 and R_4 , which can now be computed using the Lanczos method.

Note from Eq. (41), a real solution with $0 \leq p \leq 1$ requires $R \leq 0$, which implies $R_4 < 3$ and is representative of systems approaching an asymmetric Gaussian. Note that mathematically a solution for p also exists when $R > 1$, which would imply $R_4 > 3$ with a very large asymmetry. This solution, however, does not yield a physical solution where the R_3 and R_4 moments of the binomial correspond to the actual moments. Thus, the binomial is not applicable to the ^{76}Ge results shown in Sec. V A.

In Fig. 11, results for the level density and cumulative density for the $J^\pi = 1/2^-$ and $25/2^-$ states in ^{57}Fe are shown for the binomial approximation (green lines) and are compared to the ELM(8,100) (blue lines) and the shell model (black lines) obtained with a finite number of Lanczos

iterations as specified in the figures. The figures show that both ELM and the binomial approximation are in agreement at higher excitation energies where the density of states is quite high. At lower excitation energies, the binomial approximation can be poor since it lacks information about the ground state and the low-lying spectrum, and in the case for the $J^\pi = 1/2^-$ state in ^{57}Fe , the “effective” lowest energy lies above the shell-model state. This is not surprising since the binomial is limited to only four moments, and as was already pointed out, one would need of the order 40 moments (20 Lanczos iterations) for a reasonable calculation of the ground-state energy. In addition, the low-energy behavior of the binomial is Gaussian-like, and thus, the level density tends to decrease dramatically at low energy, giving an effective lowest state so that $E_0^{\text{eff}} > E_0$. For the most part, the ELM procedure can provide a better description of the low-lying spectrum if sufficient Lanczos iterations are performed to determine the energy of the lowest state in the specified model space.

C. Analytic continuation of the level density

As is shown in the previous sections, the level density modeled from the moments and shifted relative to the exact ground-state energy is a good representation of the exact shell-model level density at higher excitation energies. The principal question, however, is how to properly describe the level density in the situations illustrated in Fig. 10 where the ELM has a discontinuity in the Lanczos matrix elements and Fig. 11 where the binomial approximation substantially undershoots the shell-model result. In both cases, the moments by themselves dramatically miss the lowest energy, E_0 in the configuration space, leading to an “effective” E_0^{eff} that is too high in energy. In principle, the ELM($8, N_{\text{Lanc}}$) procedure will work by ensuring that the modeled and exact Lanczos matrix elements are reasonably matched so that there is not a discontinuity larger than natural noise in the calculated matrix elements. In some cases, however, the number of Lanczos iterations, N_{Lanc} required would be prohibitively large, which in effect negates any advantages in the approach.

A strategy for the case when $E_0^{\text{eff}} > E_0$ is similar to that outlined by Gilbert and Cameron [25] where the goal was to describe the level density via two components: an exponentially increasing function at low energy that is then matched to the back-shifted Fermi gas at higher energies. Here, we take a similar approach by matching an exponentially increasing level density to the ELM level density at a matching energy E_m . Thus, at low energy, the density of states is taken to be

$$\rho(E_x) = \exp[(E_x - E_{\text{shift}})/T]. \quad (43)$$

Note that E_{shift} specifies that for the cumulative density we have $N(E_{\text{shift}}) = 1$. The exponential level density of Eq. (43) can then be matched at energy E_m to the ELM or binomial approximation by requiring continuity in the level density and by defining the temperature T as the inverse of the logarithmic derivative of ρ , i.e.,

$$T(E_x) = \frac{\rho(E_x)}{\rho'(E_x)}. \quad (44)$$

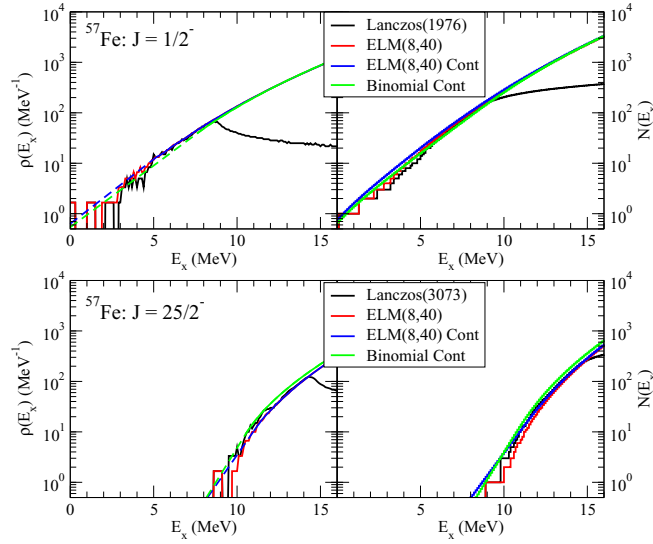


FIG. 12. Results for the level density and cumulative density for $J^\pi = 1/2^-$ and $25/2^-$ states in ^{57}Fe within the $1p0f$ shell-model space with the GXPF1A interaction. The black lines show the shell-model calculation with the specified number of Lanczos iterations. The red line denotes the ELM(8,40) result. The blue and green lines represent the $\text{ELM}_{\text{AC}}(8,40)$ and binomial calculations, as described in the text, respectively. The dashed blue and green lines indicate the region where the level density is exponential as described by Eq. (43).

At a given E_m , the continuity requirement for the level density specifies E_{shift} as

$$E_{\text{shift}}(E_m) = E_m - T(E_m) \ln[\rho(E_m)]. \quad (45)$$

Thus, the matching energy can be chosen so that $E_{\text{shift}}(E_m) = E_0$. Practical considerations for finding the matching energy for the ELM procedure are given in Appendix B.

In Fig. 12, results for the ELM analytic continuation, $\text{ELM}_{\text{AC}}(8,40)$, and the binomial level densities are shown for the $J^\pi = 1/2^-$ and $25/2^-$ states in ^{57}Fe , while the $\text{ELM}_{\text{AC}}(8,40)$ level density for the $J^\pi = 0^+$ and 4^+ states in ^{76}Ge are shown in Fig. 13 (note that the binomial approach is not applicable due to $R_4 > 3$). The dashed lines in both figures indicate the region where the level density is described by the constant-temperature, or exponential level density as described by Eq. (43). Overall, the extrapolation works well; especially when the effective lowest state for the modeled level density is higher than the actual, i.e., $E_0^{\text{eff}} > E_0$. Under this condition, it is possible to smoothly match the modeled level density down to the lowest state. As can be seen in Figs. 12 and 13, however, in some cases, such as for lower spins, the extrapolated level density tends to miss a ‘‘gap’’ in the excitation spectrum at low excitation energies. This most likely reflects the effect of pairing.

The case where $E_0^{\text{eff}} < E_0$ is less common and is generally not possible with the binomial level density due to the high curvature of the Gaussian, which tends to decrease the level density dramatically at low excitation energy. However, this can occur for the ELM when a small number of actual Lanczos iterations, N_{Lanc} , is used. However, for ELM, better agreement

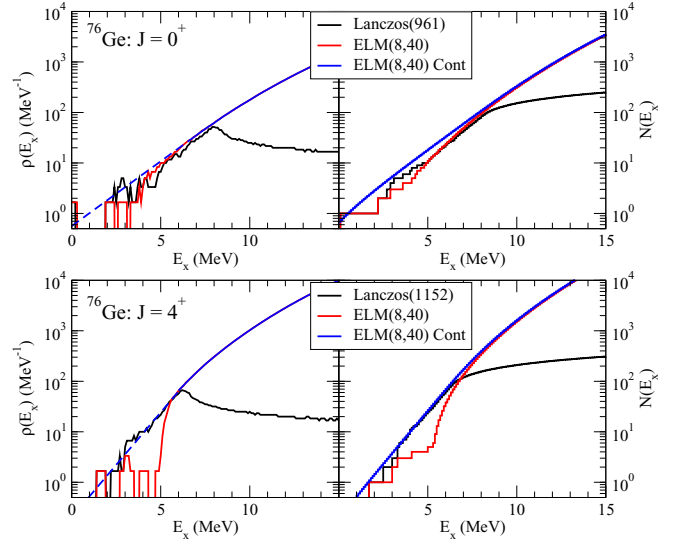


FIG. 13. Results for the level density and cumulative density for $J^\pi = 0^+$ and 4^+ states in ^{76}Ge within the $jj44$ shell-model space with the $jj44b$ interaction. The black lines show the shell-model calculation with the specified number of Lanczos iterations. The red and blue lines represent ELM(8,40) and the $\text{ELM}_{\text{AC}}(8,40)$ as described in the text, respectively. The dashed blue and green lines indicate the region where the level density is exponential as described by Eq. (43).

with the low-lying spectrum is achieved with increasing N_{Lanc} , which is also needed to obtain a reasonable estimate of E_0 . Shown in Fig. 14 is the case of the $J^\pi = 15/2^-$ space in ^{57}Fe (within the $1p0f$ -shell model space with the GXPF1A interaction), where results for ELM(8,4) (red), ELM(8,40) (green), and ELM(8,100) (blue) are shown in comparison to

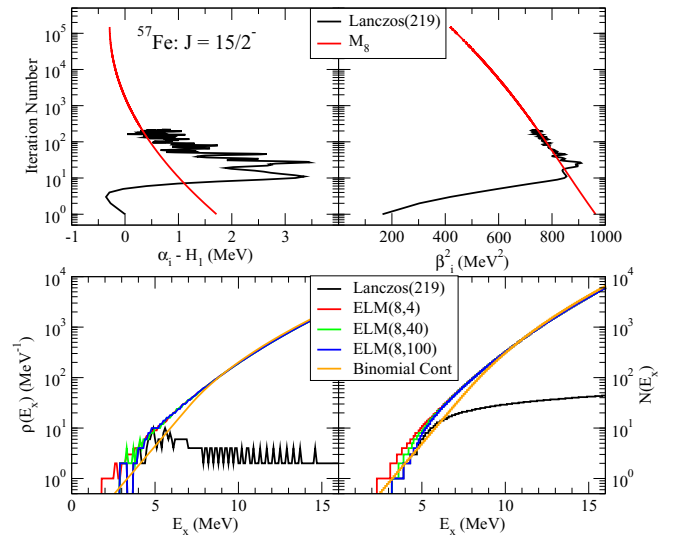


FIG. 14. Comparison of results with $\text{ELM}(8, N_{\text{Lanc}})$ for $N_{\text{Lanc}} = 4$ (red), 40 (green), and 100 (blue) for the $J^\pi = 15/2^-$ space in ^{57}Fe within the $1p0f$ -shell model space with the GXPF1A interaction. In addition the shell model with 219 Lanczos iterations (black) and the analytically continued binomial (orange) are also shown.

TABLE IV. Parameters for the $\text{ELM}_{\text{AC}}(8,40)$ calculations for the level density for ^{57}Fe and ^{76}Ge .

	J^π	T (MeV)	E_m (MeV)
^{57}Fe	$1/2^-$	1.701	7.5
	$3/2^-$	1.439	7.5
	$5/2^-$	1.345	7.5
	$7/2^-$	0.938	7.5
	$9/2^-$	1.173	7.5
	$11/2^-$	0.508	7.5
	$13/2^-$	0.955	7.5
	$15/2^-$	0.400	7.5
	$17/2^-$	0.952	7.5
	$19/2^-$	Unavailable	Unavailable
	$21/2^-$	0.813	8.3
	$23/2^-$	Unavailable	Unavailable
	$25/2^-$	0.915	11.1
	^{76}Ge	0^+	1.696
0^-		1.047	5.6
1^+		0.999	6.1
1^-		0.867	5.3
2^+		1.236	6.4
2^-		0.884	5.5
3^+		0.889	3.5
3^-		0.751	5.8
4^+		0.995	5.9
4^-		0.830	4.7
5^+		0.829	6.4
5^-		0.775	5.5
6^+		0.972	6.8
6^-		0.747	4.6
7^+		0.766	6.3
7^-		0.693	5.3
8^+	0.474	3.7	
8^-	0.695	6.8	

the shell model with 219 Lanczos iterations (black) and the analytically continued binomial approximation (orange). All the modeled level densities are in agreement at high energy, where the spectrum is dominated by the statistical properties of the Hamiltonian. The agreement between $\text{ELM}(8, N_{\text{Lanc}})$ and the shell model at low excitation energy improves with increasing N_{Lanc} as is to be expected. Indeed, reasonable agreement is achieved with $\text{ELM}(8,40)$ which is close to the minimum number of iterations needed to give an accurate energy for E_0 and the next level.

Shown in Table IV are the parameters T (temperature) and E_m (matching energy) for the ELM_{AC} calculations for level density for ^{57}Fe and ^{76}Ge described earlier for each angular momentum and parity. In each case, E_0 is the lowest energy for each configuration space. We note that for ^{57}Fe both the $19/2^-$ and $23/2^-$ configuration spaces, the analytic continuation is not applicable (labeled as unavailable). For these cases, the $\text{ELM}(8,40)$ level density rises very rapidly giving the condition $E_m = E_0$ with $T = 0$.

Shown in Fig. 15 are results for the various approaches for the summed over angular momenta with fixed parity. The black lines show the results from the Lanczos iterations while the red lines are the $\text{ELM}(8,100)$ results. The blue lines show

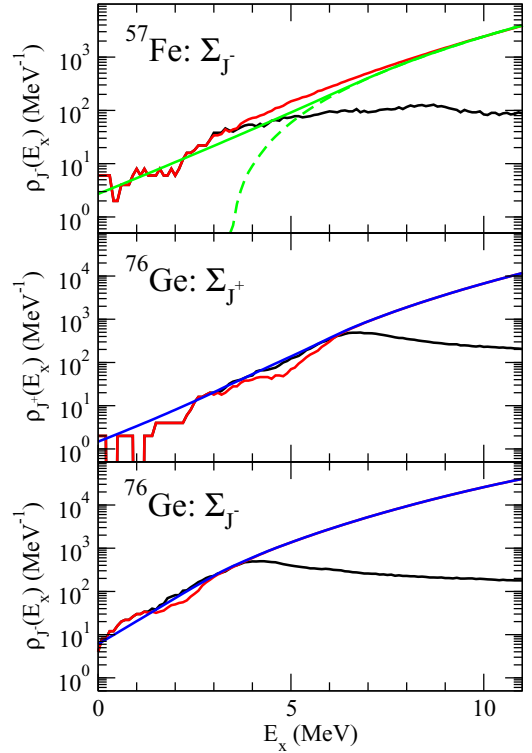


FIG. 15. Comparison of results of the level density summing all angular momenta of a given parity for ^{57}Fe (Σ_{J^-}), ^{76}Ge (Σ_{J^+}), and ^{76}Ge (Σ_{J^-}). The black lines are from the Lanczos iterations, the red line is the $\text{ELM}(8,100)$ reconstruction, the blue and green lines are $\text{ELM}_{\text{AC}}(8,40)$ results. The dashed green line is from the binomial, while the green line is the analytic continuation of the binomial. (^{57}Fe only).

the $\text{ELM}_{\text{AC}}(8,40)$ results. The green line is the result for the analytically continued binomial, while the dashed green line is the binomial (^{57}Fe only). For the most part, both the ELM and binomial agree at high excitation energy. In general, the most successful approach is $\text{ELM}(8, N_{\text{Lanc}})$ where N_{Lanc} is large enough to capture key features of the Lanczos matrix elements. As discussed previously, this is when the difference between the modeled and actual Lanczos matrix elements is less than the natural “noise” in the matrix elements; that is no strong discontinuities. For ^{57}Fe , this is generally achieved with $N_{\text{Lanc}} \approx 50-100$. In this sense, the $\text{ELM}(8,100)$ results are likely representative of the full shell model with 150 000 iterations. For ^{57}Fe , analytically continuing the binomial to E_0 is a significant improvement over the binomial itself. It does, however, tend to underestimate the actual level density in the region $E_x \approx 3-8$ MeV. For ^{76}Ge , one would need $N_{\text{Lanc}} \geq 1000$ to avoid the most significant discontinuities. A situation that is less than ideal. However, analytically continuing the $\text{ELM}(8,40)$ gives a good overall description of the level density.

VI. APPLICATIONS OF THE ELM: ^{57}Fe , ^{74}Ge , and ^{76}Ge

We now apply the extrapolated Lanczos method to compute the level density for ^{57}Fe within the $0p1f$ model space

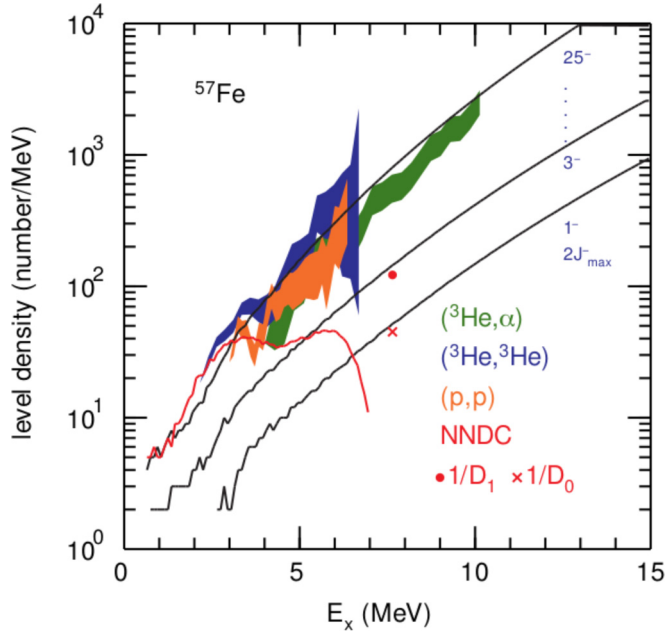


FIG. 16. Level densities for ^{57}Fe . The black lines show the calculated angular-momentum summed level density for negative-parity states up to the value of $2J_{\text{max}}^{\pi}$ as indicated to the right of each line. The experimental $\ell = 0$ and 1 level densities [27] at $E_x = S_n$ are shown by the red cross and circle, respectively, with error bars about the size of the symbols. Note that the calculated level densities are only for the negative parity states contained within the $1p0f$ shell model space. Other data is for the sum of both negative and positive parity states. The red line shows the experimental level density obtained from the states listed in NNDC [28]. Level densities inferred from reaction data are shown by the shaded areas: (green) $^{55}\text{Mn}(^3\text{He}, \alpha)$ reaction [30], (blue) $^{57}\text{Fe}(^3\text{He}, ^3\text{He}')$ reaction [29], and (orange) $^{57}\text{Ni}(p, p')$ reaction [31].

using the GXPF1A interaction. The level densities for each negative parity, angular momentum configuration space were computed with ELM(8,100) and are shown in Fig. 16. The black lines show the angular-momentum summed level density for negative parity states up to the $2J_{\text{max}}^{\pi}$ value indicated to the right of each line. The experimental $\ell = 1$ level density [27] ($\rho_{1/2^-} + \rho_{3/2^-}$) at $E_x = S_n$ (the neutron decay threshold) is shown with the red circle (the error bar is approximately equal to the size of the circle). The experimental value for $\ell = 0$ level density [27] ($\rho_{1/2^+}$) at $E_x = S_n$ is shown with the red cross (the error bar is approximately equal to the size of the cross). Other data shown in the figure is for the sum of both positive and negative parity states. The red line shows the level density obtained from the experimentally observed states listed in the NNDC [28]. The shaded areas are the bounds inferred from the various reaction data (see Fig. 16 caption) [29–31]. We note that the $1p0f$ shell model space does not contain any positive parity states for ^{57}Fe .

The agreement between our calculation (the sum of densities for states with $1/2^-$ and $3/2^-$) and the $\ell = 1$ level density is excellent. In addition, the level density for $1/2^+$ states is nearly the same as that computed for $1/2^-$ states, which indicates that the parity ratio is close to unity at $E_x = S_n$. Thus,

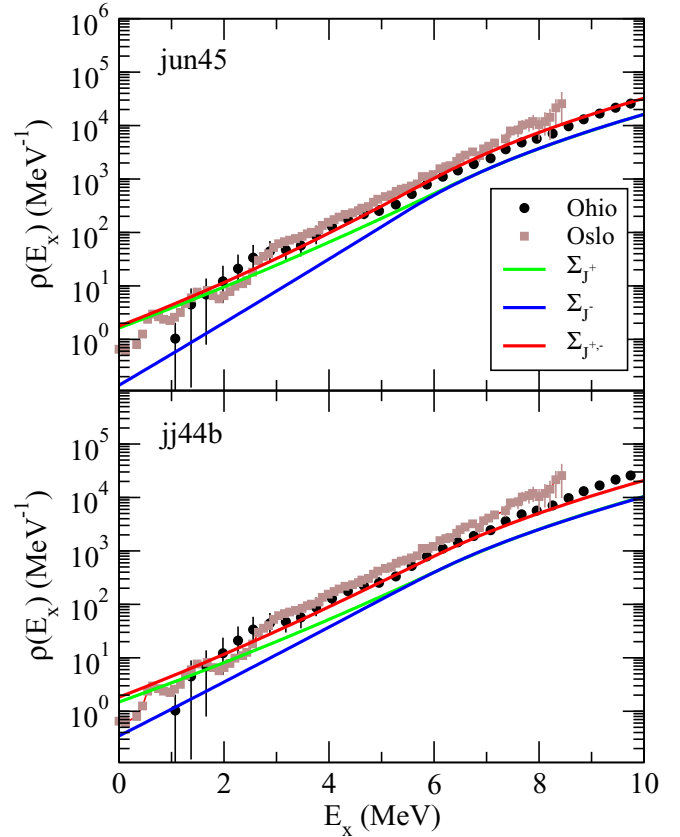


FIG. 17. Level densities for ^{74}Ge compared with experimental values. The black points, labeled Ohio, are inferred from proton evaporation spectra [32], while the brown squares, labeled Oslo, are from the Oslo method [33]. Level densities are shown for two shell model interactions, jun45 (upper) and jj44b (lower). The green and blue lines represent the total level density for positive- and negative-parity states, respectively, while the red line is the total level density.

our estimate of the total level density would be a factor of two larger than shown in Fig. 16. The level density obtained from NNDC [28] levels (see Fig. 16) becomes about a factor of two larger than that calculated for negative parity states starting around $E_x = 3$ MeV, indicating a parity ratio close to unity around 3 MeV. Taking this into account, the total level density above 3 MeV should be a factor of two larger than that for negative parity states alone. The overall agreement between the calculated level density and that inferred from reaction data is reasonable. However, the differences exhibited between the different reactions and the fact that the inferred level densities are of the order as those computed here suggest that each reaction might be more selective than expected and the analysis is potentially missing states.

A proper treatment of the $1/2^+$ level density for Fe nuclei must take into account particle-hole excitations beyond the $1p0f$ model space. For example, for ^{57}Fe we should consider the coupling of the $\nu(0g_{9/2})$ particle orbital to the calculated level density of $(4,5)^+$ states of ^{56}Fe , and the coupling of $\pi(0d_{3/2}, 1s_{1/2})$ hole orbitals to the calculated level density of

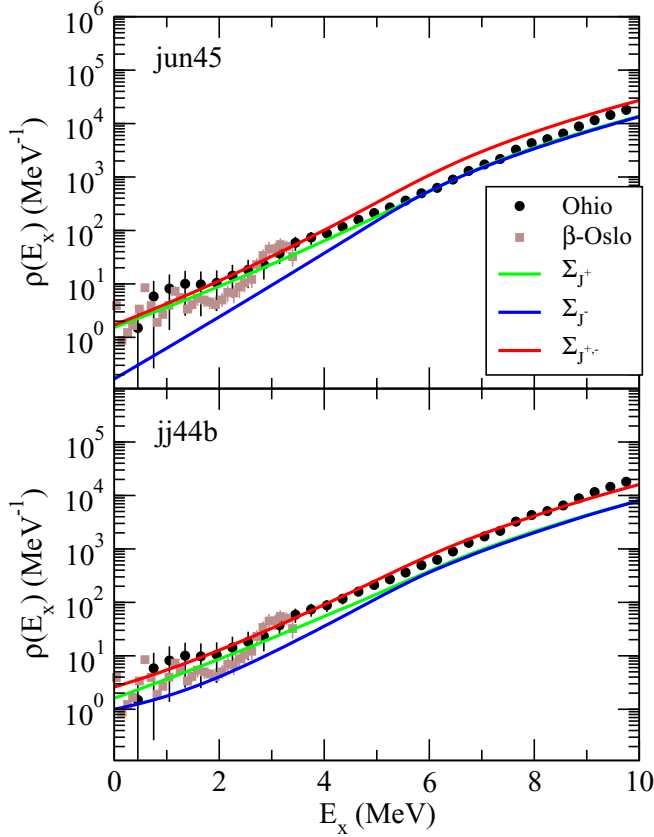


FIG. 18. Level densities for ^{76}Ge compared with experimental values. The black points, labeled Ohio, are inferred from proton evaporation spectra [32], while the brown squares, labeled Oslo, are from the β -Oslo method [34]. Level densities are shown for two shell model interactions, jun45 (upper) and $jj44b$ (lower). The green and blue lines represent the total level density for positive- and negative-parity states, respectively, while the red line is the total level density.

$(0,1,2,3)^+$ states of ^{58}Co . This extension will be explored in the future.

In Figs. 17 and 18, the $\text{ELM}_{\text{AC}}(8,100)$ results are shown for the nuclei ^{74}Ge and ^{76}Ge within the $jj44$ shell-model space and the $jj44b$ and jun45 interactions in comparison with experimental values inferred from proton evaporation spectra resulting from the compound nuclear reactions $^{68,70}\text{Zn}(^7\text{Li}, \text{Xp})$ (black circles) [32]. In addition, for ^{74}Ge , results [33] from the Oslo method are shown (brown squares), while for ^{76}Ge , results [34] from the β -Oslo method are shown. The Oslo method requires two parameters for the normalization given in Eq. (5) of Ref. [33]. Details of the methods for determining these parameters are discussed in Ref. [33]. Overall, the agreement between the $\text{ELM}_{\text{AC}}(8,100)$ results and those inferred from proton-evaporation spectra are excellent up to $E_x \approx 8-9$ MeV. This is well within the expectation that the shell model provides an accurate representation of the excitation spectrum up to the point where intruder states appear.

To conclude this section, calculated values for the level spacings for Fe and Ge isotopes are shown in Tables V and VI, respectively. For Fe isotopes, level spacing for $l = 1$

TABLE V. Comparison between calculated and experimental [27] level spacings for $l = 1$ neutron resonances (D_1) for various Fe isotopes. The neutron separation energy, S_n , for the isotope of listed and the angular momentum J_i^π for the target $A-1$ Fe nucleus are shown.

	J_i^π	S_n (MeV)	D_1^{calc} (keV)	D_1^{exp} (keV)
^{55}Fe	0^+	9.298	5.6	4.75 ± 0.15
^{57}Fe	0^+	7.646	7.6	8.21 ± 0.48
^{58}Fe	$\frac{1}{2}^-$	10.044	3.3	2.58 ± 0.26
^{59}Fe	0^+	9.298	11.6	5.03 ± 0.30

neutron resonances, D_1 , are shown, while for Ge isotopes, the level spacings for $l = 0$ neutron resonances are displayed. The experimental neutron separation energy, S_n , which is equivalent to the excitation energy of the system of interest, is tabulated as well as the angular momentum and parity, J_i^π , of the target $A - 1$ nucleus. The experimental data are from Ref. [27]. For the Ge isotopes, results are shown for the two shell-model Hamiltonians $jj44b$ and jun45. Overall, good agreement is achieved for Fe isotopes except for ^{59}Fe , which is likely signaling an increasing importance of the $0g_{9/2}$ orbit as more neutrons are added. For the Ge isotopes, the calculated D_0 values are larger than experiment. This implies that the computed level densities are too small, which is in contradiction with the agreement with the level densities inferred from proton-evaporation spectra as shown in Figs. 17 and 18. The jun45 interaction has a larger level density and generally yields a D_0 value within a factor of two from experiment. The exception is ^{74}Ge , but here $S_n = 10.196$ MeV, which from Fig. 17, is an excitation energy about 1–2 MeV above where the model space is valid. However, we note the overall good agreement between our Ge calculations and the data from Ref. [32] shown in Figs. 17 and 18.

VII. ANGULAR MOMENTUM DEPENDENCE OF THE LEVEL DENSITY

The angular momentum dependence of the level density is key to understanding many reactions. A commonly used form comes from the original work of Bethe [35], where the level density for a given J is

$$\rho(E_x, J) = P(J)\rho(E_x), \quad (46)$$

TABLE VI. Comparison between experimental [27] and calculated (with the $jj44b$ and jun45 interactions) level spacings for $l = 0$ neutron resonances (D_0) for various Ge isotopes. The neutron separation energy, S_n , for the isotope of listed and the angular momentum J_i^π for the target $A-1$ Ge nucleus are shown.

	J_i^π	S_n (MeV)	D_0^{calc} (keV) $jj44b$	D_0^{calc} (keV) jun45	D_0^{exp} (keV)
^{73}Ge	0^+	6.782	6.6	4.3	2.07 ± 0.29
^{74}Ge	$\frac{9}{2}^+$	10.196	0.33	0.23	0.099 ± 0.001
^{75}Ge	0^+	6.505	8.9	5.5	3.0 ± 1.5
^{77}Ge	0^+	6.076	18.14	10.6	4.82 ± 0.76

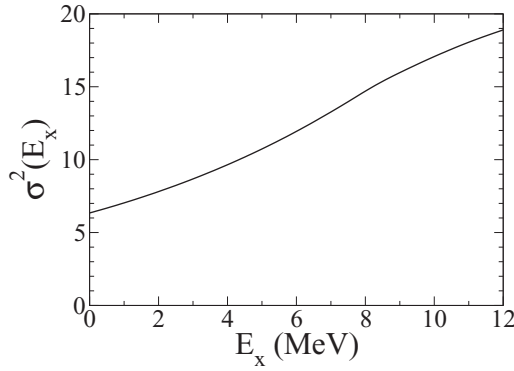


FIG. 19. Calculated spin cutoff parameter for ^{57}Fe as a function of excitation energy.

with

$$P(J) = \frac{(2J+1)}{2\sigma^2} \exp[-(J+1/2)^2/2\sigma^2], \quad (47)$$

and σ^2 being the so-called spin cutoff parameter, which is energy dependent. The spin cutoff parameter can be determined at a fixed excitation energy via

$$\sigma^2 = \langle (J+1/2)^2 \rangle / 2. \quad (48)$$

The calculated spin cutoff parameters for ^{57}Fe , ^{74}Ge , and ^{76}Ge as a function of excitation energy are shown in Figs. 19 and 20. In Fig. 20, both the positive- and negative-parity spin cutoff parameters are shown.

The probability distribution of angular momenta for the three nuclei studied are shown in Figs. 21–23 at five distinct

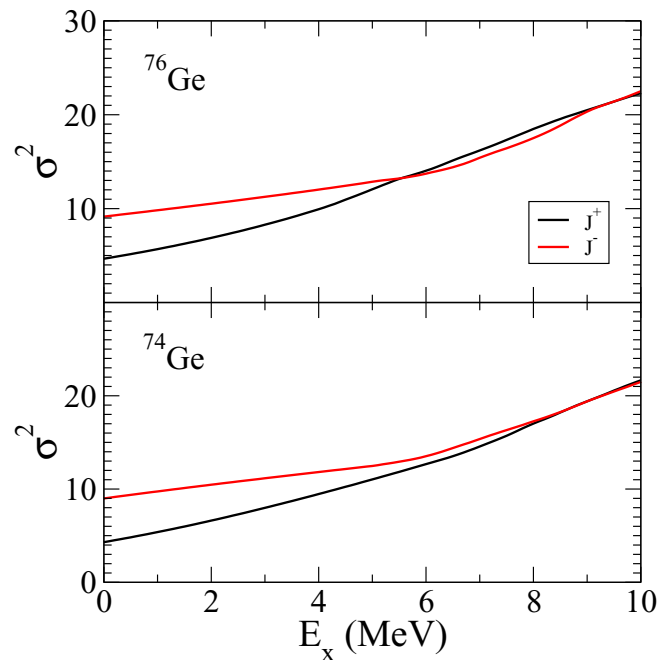


FIG. 20. Calculated spin cutoff parameter for ^{74}Ge and ^{76}Ge as a function of excitation energy. The black and red lines represent the positive- and negative-parity spaces, respectively.

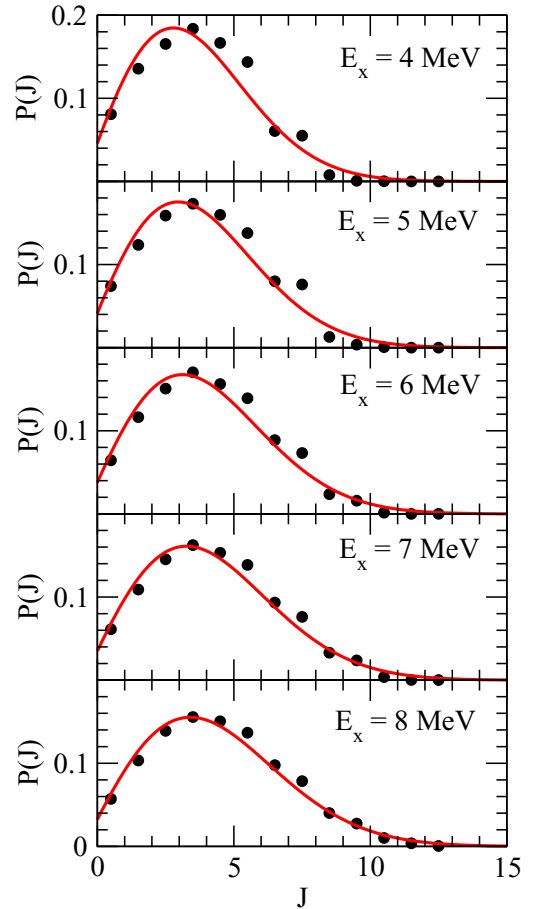


FIG. 21. Angular momenta probabilities for ^{57}Fe are shown for five excitation-energy slices across the density of states. The red lines show the results obtained from Eq. (47) with the spin cutoff parameter shown in Fig. 19.

excitation energies. The black points are the probability distributions from the extrapolated Lanczos method, while the red lines represent the results from Eq. (47) using the spin cutoff parameters computed at each excitation energy as shown in Figs. 19 and 20. Overall, the computed angular momenta distributions are in excellent agreement with the Bethe ansatz of Eq. (47) and the shell-model calculations for the even-even nuclei show an odd-even staggering in angular momentum at lower excitation energies.

We note that the effect of angular momentum on the level density for Fe isotopes was also investigated in detail with the Shell Model, Monte Carlo approach [36] in the $0f1p + 0g_{9/2}$ model space with a schematic good-sign Hamiltonian. More will be done with our ELM approach using realistic Hamiltonians and extending the space to also include proton holes in the sd shell.

VIII. CONCLUSIONS

We have discussed the application of the Lanczos method to the calculation of level densities. We showed that for a given J value, the α_{1-4} and β_{1-4} components of the Lanczos matrix obtained from the first four Lanczos iterations provide

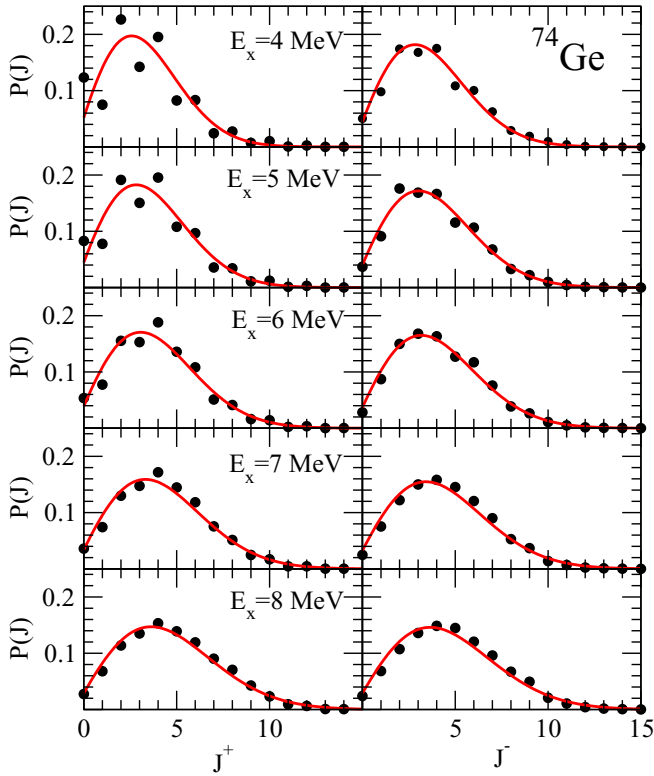


FIG. 22. Angular momenta probabilities for ^{74}Ge are shown for five excitation energies across the positive- and negative-parity states. The red lines show the results obtained from Eq. (47) with the spin cutoff parameter shown in Fig. 20.

the information sufficient to obtain the lowest eight moments of the Hamiltonian with an accuracy of approximately 1%. We derive exact but complex equations that relate these α and β matrix elements to the moments. We compare the results to calculations for matrix dimensions up to 10^6 where exact results from full diagonalization can be obtained. We also show that the uncertainty of the moments decreases with increasing matrix dimension.

A method to extrapolate the Lanczos matrix (ELM) to the full space was presented that made use of the first eight moments of the Hamiltonian. Level densities were obtained with the ELM method and compared to exact shell-model results where possible. The ELM procedure was shown to provide an excellent representation of the asymptotic (high-energy) behavior of the level density, and with a sufficient number of actual Lanczos iterations, the ELM method was shown to provide excellent agreement with the exact shell-model level density. In some cases, a discontinuity exists between the exact Lanczos iterations and the modeled matrix elements that causes the ELM procedure to miscalculate the level density at low excitation energies. A procedure to analytically continue the level density from the high-energy region to the lowest energy in the configuration space (E_0) was presented. A calculated uncertainty of about 100(10) keV in the ground-state energy is enough to obtain the level density above with an accuracy of approximately 10(1)% for a given model space and Hamiltonian. The calculation of

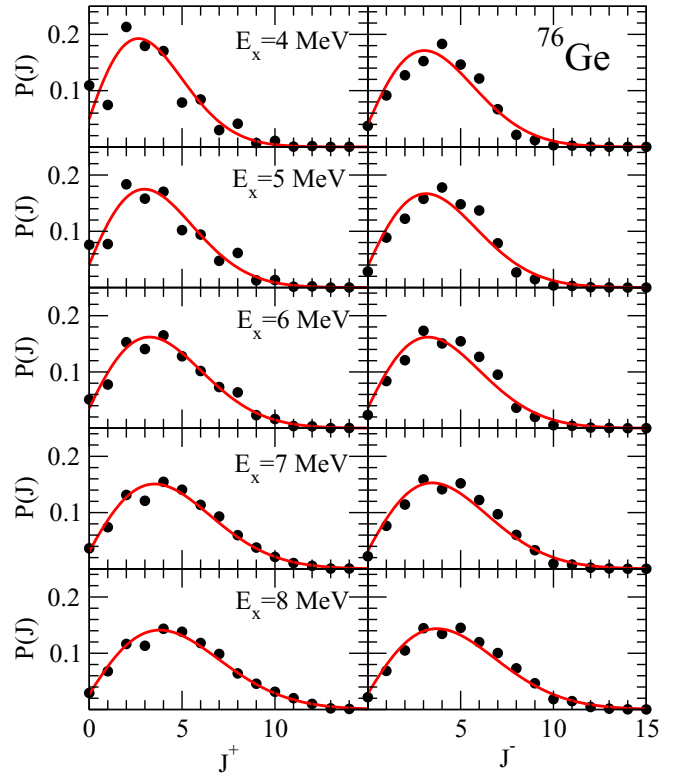


FIG. 23. Angular momenta probabilities for ^{76}Ge are shown for five excitation energies for positive- and negative-parity states. The red lines show the results obtained from Eq. (47) with the spin cutoff parameter shown in Fig. 20.

the ground-state energy to within 100 keV requires on the order of 20 Lanczos iterations.

We compare the results of the ELM method with those obtained with the binomial approximation that makes use of the first four moments. In some cases with the moments close to the Gaussian limit, the two methods give similar results. But there are other cases with the binomial method cannot be used. Finally, we compared calculations for the level density with ELM for ^{57}Fe and $^{74,76}\text{Ge}$ nuclei with those extracted from experiment. In addition, we computed $\ell = 0$ and 1 resonance spacing, D_0 and D_1 , for Fe and Ge isotopes.

ACKNOWLEDGMENTS

We gratefully acknowledge several useful discussions with S. Grimes, A. C. Larsen, Z. Meissel, A. Voinov, and K. Wendt. W.E.O. performed this work under the auspices of the US Department of Energy by Lawrence Livermore National Laboratory under Contract No. DE-AC52-07NA27344 with support from the Office of Nuclear Physics under Field Work Proposal No. SCW0498. B.A.B. acknowledges support from the National Science Foundation under Grant No. PHY-1811855.

APPENDIX A: SOLUTION FOR a AND b PARAMETERS

Given the set of moments H_1 , M_2 , and R_{3-8} , the strategy is then to find an optimal set of coefficients a_i and b_i that

reproduce these moments. From Eqs. (31)–(35), it is clear that the moments are highly nonlinear functions of the parameters a_i and b_i . However, in general, the dominant parameters will be a_0 and b_1 . For example, in the limit of a Gaussian, the odd moments are zero, and $M_2 = -2b_1$. Thus, one strategy to find the parameters is to assume that a_{1-3} and b_{2-4} are small and that the moments can be linearized relative to small changes in the parameters. We start with all $a_{i>0} = 0$ and solve for b_1 and b_2 using M_2 and M_4 . Note that b_2 can be isolated with the ratio M_4/M_2^2 , yielding a quadratic equation with two solutions, with the smallest being the most realistic. With b_2 found, we then use M_2 to fix b_1 . Initial estimates for a_1 and a_2 can then be found from the odd moments M_3 and M_5 by truncating the analytic expressions to the leading linear terms in a_1 and a_2 , yielding two coupled linear equations:

$$M_3 \approx 6b_1[a_1(1 - 4b_2) - 4a_2(1 - 5b_2)], \quad (\text{A1})$$

$$M_5 \approx 120b_1^2[a_1(3 + 24b_2^2) - a_2(9 + 168b_2^2)]. \quad (\text{A2})$$

With these initial estimates, we then perform a Taylor expansion for the moments and truncate to first order. Representing the parameters a_i and b_i with the combined parameters, p_i , and using vector notation $\vec{p} = \{\vec{a}, \vec{b}\}$, a set of coupled linearized expressions for the moments can be obtained, i.e.,

$$M_k - M_k(\vec{p}) = \sum_i D_{ki} \Delta p_i, \quad (\text{A3})$$

where M_k is the moment for shell-model Hamiltonian and $M_k(\vec{p})$ is the modeled moment evaluated from Eqs. (22)–(29)

using the modeled Lanczos matrix elements α_i and β_i from Eqs. (20) and (21). $D_{ki} = \frac{\partial M_k}{\partial p_i}$ is the derivative of the k^{th} moment with respect to parameter p_i . Under the conditions that the nonlinear terms are small, one can iteratively obtain the optimal parameters \vec{p} by solving for the shift $\Delta\vec{p}$ and updating the derivative matrix after each iteration. To minimize potential effects of nonlinear terms, at each iteration a fraction of the shift is taken to update the new values. In practice, half the new value was chosen, and the procedure typically finds optimal solutions in approximately 20 iterations.

APPENDIX B: FINDING THE MATCHING ENERGY FOR THE ELM

Finding the matching energy E_m to analytically continue the ELM calculation of the level density is complicated by local fluctuations in the level density due to the discrete nature of the spectrum. Thus, it is necessary to introduce a smoothing procedure to make use of Eqs. (44) and (45). In this work, we made use of a low-pass filter, or Savitsky-Golay filter [37], to both smooth and compute the derivative of the level density. To first order, the Savitsky-Golay filter is essentially a least-squares fit of polynomial of order M to the data of interest over a region of data extending n_L and n_R points to the left and right of the data point of interest respectively. Here, satisfactory results were obtained by smoothing the level density directly (not the logarithm) with $M = 4$ over the interval defined by $n_L = n_R = 10$.

-
- [1] M. Burbidge, G. Burbidge, W. Fowler, and F. Hoyle, *Rev. Mod. Phys.* **29**, 547 (1957).
- [2] D. Kasen, B. Metzger, J. Barnes, E. Quataert, and E. Ramirez-Ruiz, *Nature* **551**, 80 (2017).
- [3] J. E. Escher, J. T. Burke, F. S. Dietrich, N. D. Scielzo, I. J. Thompson, and W. Younes, *Rev. Mod. Phys.* **84**, 353 (2012).
- [4] W. Hauser and H. Feshbach, *Phys. Rev.* **87**, 366 (1952).
- [5] S. Goriely, M. Samyn, and J. M. Pearson, *Phys. Rev. C* **75**, 064312 (2007); S. Goriely, S. Hilaire, and A. J. Koning, *ibid.* **78**, 064307 (2008).
- [6] C. W. Johnson, S. E. Koonin, G. H. Lang, and W. E. Ormand, *Phys. Rev. Lett.* **69**, 3157 (1992).
- [7] G. H. Lang, C. W. Johnson, S. E. Koonin, and W. E. Ormand, *Phys. Rev. C* **48**, 1518 (1993).
- [8] S. E. Koonin, D. J. Dean, and K. Langanke, *Phys. Rep.* **278**, 1 (1997); H. Nakada and Y. Alhassid, *Phys. Rev. Lett.* **79**, 2939 (1997); W. E. Ormand, *Phys. Rev. C* **56**, R1678 (1997); Y. Alhassid, S. Liu, and H. Nakada, *Phys. Rev. Lett.* **83**, 4265 (1999); H. Nakada and Y. Alhassid, *Phys. Rev. C* **78**, 051304(R) (2008); C. Özen, Y. Alhassid, and H. Nakada, *ibid.* **91**, 034329 (2015).
- [9] K. K. Mon and J. B. French, *Ann. Phys.* **95**, 90 (1975); S. S. M. Wong and J. B. French, *Nucl. Phys. A* **198**, 188 (1972); J. B. French and V. K. B. Kota, *Annu. Rev. Nucl. Part. Sci.* **32**, 35 (1982); *Phys. Rev. Lett.* **51**, 2183 (1983); Z. Pluhar and H. A. Weidenmüller, *Phys. Rev. C* **38**, 1046 (1988).
- [10] A. P. Zuker, *Phys. Rev. C* **64**, 021303(R) (2001).
- [11] R. A. Sen'kov and M. Horoi, *Phys. Rev. C* **82**, 024304 (2010).
- [12] R. A. Sen'kov, M. Horoi, and V. G. Zelivinsky, *Comput. Phys. Commun.* **184**, 215 (2013).
- [13] N. Shimizu, Y. Utsuno, Y. Futamura, T. Sakurai, T. Mizusaki, and T. Otsuka, *Phys. Lett. B* **753**, 13 (2016).
- [14] B. Jegerlehner, Report No. IUHET-353, [arXiv:hep-lat/9612014](https://arxiv.org/abs/hep-lat/9612014).
- [15] S. Yamamoto, T. Sogabe, T. Hoshi, S.-L. Zhang, and T. Fujiwara, *J. Phys. Soc. Jpn.* **77**, 114713 (2008).
- [16] R. D. Lawson, *Theory of the Nuclear Shell Model* (Clarendon, Oxford, 1980); P. J. Brussaard and P. W. M. Glaudemans, *Shell Model Applications in Nuclear Spectroscopy* (North-Holland, Amsterdam, 1977).
- [17] C. Lanczos, *J. Res. Nat. Bur. Stand.* **45**, 255 (1950); J. H. Wilkinson, *The Algebraic Eigenvalue Problem* (Clarendon, Oxford, 1965); R. R. Whitehead, A. Watt, B. J. Cole, and I. Morrison, *Adv. Nucl. Phys.* **9**, 123 (1977).
- [18] A. P. Zuker, L. Waha Ndeuna, F. Nowacki, and E. Caurier, *Phys. Rev. C* **64**, 021304(R) (2001); E. Caurier, G. Martinez-Pinedo, F. Nowack, A. Poves, and A. P. Zuker, *Rev. Mod. Phys.* **77**, 427 (2005).
- [19] B. A. Brown and W. D. M. Rae, *Nucl. Data Sheets* **120**, 115 (2014).
- [20] M. Honma, T. Otsuka, B. A. Brown, and T. Mizusaki, *Eur. Phys. J. A* **25** Suppl. 1, 499 (2005).
- [21] S. Mukhopadhyay, B. P. Crider, B. A. Brown, S. F. Ashley, A. Chakraborty, A. Kumar, M. T. McEllistrem, E. E. Peters, F. M. Prados-Estévez, and S. W. Yates, *Phys. Rev. C* **95**, 014327 (2017).

- [22] M. Honma, T. Otsuka, T. Mizusaki, and M. Hjorth-Jensen, *Phys. Rev. C* **80**, 064323 (2009).
- [23] R. R. Whitehead, in *Theory and Applications of Moment Problems in Many Fermion Systems*, edited by B. J. Dalton, S. M. Grimes, J. D. Vary, and S. A. Williams (Plenum, London, 1980), p. 235.
- [24] W. E. Ormand, *Int. J. Mod. Phys.* **14**, 67 (2005).
- [25] A. Gilbert and A. G. W. Cameron, *Can. J. Phys.* **43**, 1446 (1965).
- [26] B. A. Brown and W. E. Ormand, in *Proceedings of the 15th International Conference on Nuclear Reaction Mechanisms*, edited by F. Cerutti, A. Ferrari, T. Kawano, F. Salvat-Pujol, and P. Talou, CERN-Proceedings-2019-001 (CERN, Geneva, 2019), pp. 21–28.
- [27] S. Mughabghab, *Atlas of Neutron Resonances*, Volume 1: Resonance Properties and Thermal Cross Sections $Z = 1-60$ (Elsevier, Amsterdam, 2018), 6th ed.
- [28] Data from the NNDC On-Line Data Service database as of August 2017, <http://nndc.bnl.gov/nudat2/>.
- [29] E. Algin *et al.*, *Phys. At. Nucl.* **70**, 1634 (2007).
- [30] A. Voinov *et al.*, *Phys. Rev. Lett.* **93**, 142504 (2004).
- [31] A. C. Larsen *et al.*, *J. Phys. G* **44**, 064005 (2017); (private communication) (2018).
- [32] A. V. Voinov *et al.*, *Phys. Rev. C* **99**, 054609 (2019).
- [33] T. Renstrøm, H.-T. Nyhus, H. Utsunomiya, R. Schwengner, S. Goriely, A. C. Larsen, D. M. Filipescu, I. Gheorghe, L. A. Bernstein, D. L. Bleuel, T. Glodariu, A. Gørgen, M. Guttormsen, T. W. Hagen, B. V. Kheswa, Y.-W. Lui, D. Negi, I. E. Ruud, T. Shima, S. Siem, K. Takahisa, O. Tesileanu, T. G. Tornyi, G. M. Tveten, and M. Wiedeking, *Phys. Rev. C* **93**, 064302 (2016).
- [34] A. Spyrou, S. N. Liddick, A. C. Larsen, M. Guttormsen, K. Cooper, A. C. Dombos, D. J. Morrissey, F. Naqvi, G. Perdikakis, S. J. Quinn, T. Renstrom, J. A. Rodriguez, A. Simon, C. S. Sumithrarachchi, and R. G. T. Zegers, *Phys. Rev. Lett.* **113**, 232502 (2014).
- [35] H. A. Bethe, *Phys. Rev.* **50**, 332 (1936); *Rev. Mod. Phys.* **9**, 69 (1937).
- [36] Y. Alhassid, S. Liu, and H. Nakada, *Phys. Rev. Lett.* **99**, 162504 (2007).
- [37] A. Savitsky and M. J. E. Golay, *Anal. Chem.* **36**, 1627 (1964); R. W. Hamming, *Digital Filters*, 2nd ed. (Prentice Hall, Englewood Cliffs, NJ, 1983); M. U. A. Bromba, *Anal. Chem.* **53**, 1583 (1981); W. H. Press, S. A. Teukolsky, W. T. Vetterling, and B. P. Flannery, *Numerical Recipes in Fortran*, 2nd ed. (Cambridge University Press, New York, 1992), pp. 644–649.